May 2016

Predictability and Dynamics of Warm-Core Mesoscale Vortex Formation with the 8 May 2009 "Super Derecho" Event

Caleb Todd Grunzke
University of Wisconsin-Milwaukee

PREDICTABILITY AND DYNAMICS OF WARM-CORE MESOSCALE VORTEX FORMATION WITH THE 8 MAY 2009 "SUPER DERECHO" EVENT

by

Caleb T. Grunzke

A Thesis Submitted in

Partial Fulfillment of the

Requirements for the Degree of

Master of Science

in Mathematics

at

The University of Wisconsin-Milwaukee

May 2016

ABSTRACT

PREDICTABILITY AND DYNAMICS OF WARM-CORE MESOSCALE VORTEX FORMATION WITH THE 8 MAY 2009 "SUPER DERECHO" EVENT

by

Caleb Grunzke

The University of Wisconsin-Milwaukee, 2016
Under the Supervision of Professor Clark Evans

The predictability and dynamics of the warm-core mesovortex associated with the northern-flank of the 8 May 2009 "Super Derecho" event are examined by coupling the Advanced Research Weather Forecasting Model with the Data Assimilation Research Testbed facility. A 50-member convection-allowing EnKF ensemble was produced with 6 hourly-cycled analysis and assimilated observations. Cycled analysis started five days prior to 1200 UTC 7 May 2009, at which time the 36 h ensemble forecasts were launched.

The ensemble forecasts all attempted to produce a mesoscale convective system (MCS) but only fourteen percent produced a warm-core mesovortex-like feature similar to the intensity of the observed mesovortex. Ensemble sensitivity analysis was conducted to analyze the environmental differences between ensemble members. Six member composites were also created by selecting the members with the strongest and weakest 850 hPa circulation associated with the mesovortex during the 1000 UTC to 1400 UTC 8 May 2009 timeframe. It is found that a more amplified upstream upper-level trough a few hours prior to peak strength in the simulated mesovortex is associated with a stronger 850 hPa circulation. Cascading effects on the mesoscale from the amplification of the trough occur as the low-level jet and frontal zone magnitudes increase. More moisture is able to be transported poleward into western Kansas in

the stronger 850 hPa circulation members leading to convection initiation (CI). We hypothesize that CI must occur early enough in order for the characteristic airstreams of a MCS to converge the background cyclonic absolute vorticity and the vorticity contributions from the eddy and tilting vorticity terms of the local circulation tendency equation.

TABLE OF CONTENTS

List of Figures **v**

List of Tables **viii**

Acknowledgements **ix**

1. Introduction **1**

2. Methodology **6**
- *a. Cycled Analysis* 6
- *b. Free Forecasts* 9
- *c. Ensemble Sensitivity Analysis* 10
- *d. Composites* 12

3. Results **12**
- *a. Data Assimilation Performance* 12
- *b. Ensemble Performance* 14
- *c. Ensemble Sensitivity Analysis* 15
- *d. Composites* 18

4. Summary and Future Work **21**

5. References **51**

LIST OF FIGURES

Figure 1: Domain configuration for the methodology. Cycled analysis is conducted on the outer domain while the free forecasts utilize both. 24

Figure 2: Spatial distribution of assimilated observation platforms for the 1200 UTC 7 May 2009 analysis cycle. Observation counts are for unique observations within each platform type. 25

Figure 3: METAR (a) temperature (Kelvin), (b) specific humidity (g/kg), (c) altimeter (hPa), (d) *u* (m/s), and (e) *v* (m/s) assimilated observation statistics for 1200 UTC 2 May 2009 to 1200 UTC 7 May 2009. The dashed (solid) lines denote the prior (posterior) of the RMSE (red colored), total spread (blue colored), and bias (green colored). 26

Figure 4: Assimilated observation statistics for: radiosonde (a) temperature (Kelvin), (b) specific humidity (g/kg), (c) *u* wind (m/s), and (d) *v* wind (m/s); ACARS (e) temperature (Kelvin), (f) specific humidity (g/kg), (g) *u* wind (m/s), and (h) *v* wind (m/s); and AMV (i) *u* wind (m/s), and (j) *v* wind (m/s). The solid (dashed) lines denote the 0000 UTC 5 May 2009 (1200 UTC 7 May 2009) time of the RMSE (red colored), total spread (blue colored), and bias (green colored). 27

Figure 5: 1-km AGL derived reflectivity (dBZ) for ensemble members 1-20 at 1200 UTC 8 May 2009. 28

Figure 6: 850 hPa circulation (color-shaded; $\times 10^6$ $m^2 s^{-1}$) overlaid on 1-km AGL derived reflectivity (color contoured; dBZ) for ensemble members 1-20 at 1200 UTC 8 May 2009. 29

Figure 7: 850 hPa circulation (associated with the mesovortex) time series for the 50 ensemble members between 1000-1400 UTC 8 May 2009. The ensemble mean is denoted by the thick, black line, teal shading above (below) the ensemble mean denotes less than (greater than) one standard deviation above (below) the ensemble mean, Strong composite members (1, 10, 13, 15, 16, 26) are denoted by green lines, Weak composite members (5, 7, 18, 19, 28, 36) are denoted by red lines, all other members are denoted by grey lines, and the hourly time series of 850 hPa circulation from Evans et al. (2014) is denoted by the purple line. 30

Figure 8: Ensemble sensitivity analysis for 500 hPa geopotential height (m) at 0600 UTC 8 May 2009 with respect to 850 hPa maximum circulation at 1200 UTC 8 May 2009. Black contours denote the ensemble mean while color-shading denotes the sensitivity metric $\frac{\partial J}{\partial x}$. 31

Figure 9: Same as Fig. 8 except the analysis state variable **x** is 850 hPa *v* wind (m/s) at 0600 UTC 8 May 2009. 32

Figure 10: Same as Fig. 8 except the analysis state variable **x** is 850 hPa relative humidity (%) at 0600 UTC 8 May 2009. 33

Figure 11: Same as Fig. 8 except the analysis state variable **x** is 850 hPa potential temperature (Kelvin) at 0600 UTC 8 May 2009. 34

Figure 12: Same as Fig. 8 except the analysis state variable **x** is MUCAPE (J/kg) at 0600 UTC 8 May 2009. 35

Figure 13: Same as Fig. 8 except the analysis state variable **x** is 850 hPa *u* wind (m/s) at 0600 UTC 8 May 2009. 36

Figure 14: 500 hPa total wind (kt, color-shaded and barbs), 500 hPa geopotential height (m, black contours), and 500 hPa temperature (°C, red dashed) for (a) STRONG and (b) WEAK at 0600 UTC 8 May 2009. 37

Figure 15: RUC analysis of 500 hPa total wind (kt, color shaded and barbs), 500 hPa geopotential height (m, black contours), and 500 hPa temperature (°C, red dashed) at 0600 UTC 8 May 2009. 38

Figure 16: Same as Fig. 14 except for 850 hPa total wind (kt, color-shaded and barbs), 850 hPa geopotential height (m, black contours), and 850 hPa temperature (°C, red dashed). 39

Figure 17: Same as Fig. 15 except for 850 hPa total wind (kt, color shaded and barbs), 850 geopotential height (m, black contours), and 850 hPa temperature (°C, red dashed). 40

Figure 18: Same as Fig. 14 except for 850 hPa total wind (kt, barbs), 850 hPa geopotential height (m, black contours), temperature (°C, red dashed), and dewpoint (°C, green contours). 41

Figure 19: Same as Fig. 15 except for 850 hPa total wind (kt, barbs), 850 geopotential height (m, black contours), 850 hPa temperature (°C, red dashed), and 850 hPa dewpoint (°C, green contours). 42

Figure 20: Same as Fig. 14 except for MUCAPE (J/kg, color shaded), MUCIN [J/kg, grey hatched (lighter colors denote greater values)], and 0-6 km wind shear (kt, barbs). 43

Figure 21: Same as Fig. 15 except for MUCAPE (J/kg, color shaded), MUCIN [J/kg, grey hatched (lighter colors denote greater values)], and 0-6 km wind shear (kt, barbs). 44

Figure 22: 700 hPa Q-vector convergence ($\times 10^{-11}$ m^{-2} s^{-1}, color shaded), 500 hPa geopotential height (m, red dashed), and sea-level pressure (hPa, black contour) for (a) STRONG and (b) WEAK at 0600 UTC 8 May 2009. Negative shaded values denote Q-vector convergence. 45

Figure 23: 1-km AGL derived reflectivity (dBZ) at 0600 UTC 8 May 2009 for each individual composite member. STRONG (WEAK) members are on the left (right) half. 46

Figure 24: Plotted vertical cross-section of CAPE (J/kg, color-shaded), CIN [J/kg, grey hatched (lighter colors denote greater values)], *v*-*w* wind (m/s, vectors), isentropes (K, red contour), and cloud water mixing ratio (kg/kg, green contour) from A-B in Fig. 17 for (a) STRONG and (b) WEAK. Time is 0600 UTC 8 May 2009. 47

LIST OF TABLES

Table 1: WRF model options. 48

Table 2: DART options. 49

Table 3: Assimilated observation types, assumed observation errors, and observation windows. 50

ACKNOWLEDGEMENTS

I would like to thank my advisor Dr. Clark Evans for his un-subsiding assistance and advice, the University of Wisconsin-Milwaukee for allowing me to use their super-computer facilities, Dr. Sergey Kravtsov and Paul Roebber for being my reviewers, and Dr. Glen Romine for assistance with the cycled data assimilation system.

1. Introduction

An intense mesoscale convective system (MCS) formed over northwestern Kansas in the morning hours of 8 May 2009. This MCS caused damaging, straight-line wind gusts of up to 50 m s^{-1} and twenty-six tornadoes (seven tornadoes EF-2 or greater). The termed "Super Derecho" (Weisman et al. 2013) cost an estimated $115 million in damage as it traveled from northwestern Kansas to the southern Appalachians (Evans et al. 2014). An exceptionally unique characteristic about this convective system was that a strong, warm-core mesoscale vortex developed on its northern flank. While the "Super Derecho" was an unusual occurrence, a numerical simulation performed in real-time at the National Center for Atmospheric Research (NCAR) was able to successfully forecast the observed event (Weisman et al. 2013). This and other studies [e.g., Melhauser and Zhang (2012), Snively and Gallus (2014), Xu et al. (2015a,b)] have shown the capability of numerical models for providing skillful MCS forecasts and their related hazards in spite of imperfect initial conditions (ICs) and physical parameterization methods. It remains to be seen, however, if these skillful forecasts result from chance or instead suggest an appreciable amount of predictability exists for MCSs and their associated hazards.

Numerous studies have been conducted on the 8 May 2009 "Super Derecho." Coniglio et al. (2011) examined the environment and initial transformation of the convective system. They found that while synoptic forcing and instability were weak, a combination of mesoscale features allowed for convection initiation (CI) to occur. The colocation of high amounts of low-level moisture, steep mid-level lapse rates, and a strong LLJ fostered an environment that allowed for the convection to increase in intensity and organize into a persistent MCS. The high impact MCS occurred in an unusual environment compared to other MCS events within the central U.S. Specifically, though no individual characteristic of the environment was particularly atypical

compared to those found in association with known derecho-producing environments (e.g., Coniglio et al. 2004, 2011), the combination of all such environmental characteristics was atypical (Evans et al. 2014). Weisman et al. (2013) conducted an analysis of a high-resolution Advanced Research Weather Research and Forecasting (WRF-ARW; Skamarock et al. 2008) simulation that produced an accurate forecast of this event. They found that the bow echo initially moved east through an environment of high most-unstable convective available potential energy (MUCAPE) and strong vertical wind shear across the Central Plains. This contrasts with Coniglio et al. (2011) where it was established that the bow echo formed in an environment characterized by weak instability. Weisman et al. (2013) then displayed that the MCS moved into an environment characterized by weaker thermodynamic instability and vertical wind shear across eastern Kansas and Missouri. While doing so, an intense, warm-core mesoscale convective vortex (MCV) developed on the northern end of the bow echo. Cyclonic vertical vorticity that was originally a deep strip along and immediately behind the leading line became consolidated on the southern edge of the northernmost cell.

The development of the warm-core MCV was studied further using a circulation budget and backward trajectory-based vorticity budget analyses (Evans et al. 2014). Vertical vorticity around the edges of the MCV was initially generated by updraft tilting and subsequent cyclonic amplification of environmental streamwise vorticity and downdraft tilting and subsequent anticyclonic amplification of baroclinically-generated crosswise vorticity. The lower tropospheric rotation of the MCV increased due to the consolidation of the cyclonic vertical vorticity via large-scale convergence and expulsion of anticyclonic vertical vorticity by the diffluent descending rear inflow jet within the system's cold pool.

Xu et al. (2015a) conducted a high-resolution WRF-ARW simulation to examine the genesis of two mesovortices within the convective system's leading line. A circulation analysis displayed that the vertical vorticity of the mesovortices forms from near-surface horizontal vorticity being tilted into the vertical. Surface friction was revealed to create the near-surface horizontal vorticity. A further analysis of this simulation for the leading line mesovortices' characteristics and evolutions was performed by Xu et al. (2015b). It was found that the downward pressure perturbation force from the mesovoritices near the bow echo apex caused the rear-inflow jet to descend to the surface and locally enhance the surface winds.

Several studies have been conducted into the predictability of MCS events. Wandishin et al. (2008) studied MCS predictability in two dimensions (*x*-*z*) utilizing two sets of ensemble simulations. The first ensemble was generated using perturbations in wind speed (manifest in vertical wind shear), relative humidity, and instability from 24-h forecast errors from the North American Mesoscale model (NAM). The second ensemble was created by halving the magnitude of the 24-h NAM forecast error perturbations for the same variables. The research explored the question of the amount of confidence a forecaster could have in the occurrence of a MCS that a numerical model was forecasting one to two days in advance. Current 24-h forecast errors result in a MCS forecast success rate of seventy percent. Reducing the relative humidity perturbations leads to greater sensitivity of MCS success rate while the size of the MCS seems to be more impacted by wind speed perturbations. CAPE perturbations had the greatest impact of all the variables on maximum updraft strength likely due to CAPE being proportional to updraft intensity (Johns and Doswell 1992). While these specific findings are interesting, no one variable with reduced uncertainty would lead to an improved overall MCS forecast. Only reducing the uncertainties of all variables (wind speed, relative humidity, and instability) to

below the level of observational uncertainty greatly improves the MCS forecast success rate from the prior seventy percent to ninety percent. Wandishin et al. (2010) explored the previous research further utilizing three-dimension model simulations and found that no patterns of IC perturbations existed that led to an increased MCS forecast success rate. Instead, a grouping of the ensembles is observed with no clear patterns of forecast improvement for one variable. This showed that drawing any conclusions about MCS predictability by perturbing the ICs in three-dimensional simulations is very difficult.

An experiment involving a WRF-ARW 40-member ensemble was utilized to study the practical and intrinsic predictability at six to twenty-four hour lead time of the 9-10 June 2003 squall line and bow echo event (Melhauser and Zhang 2012). The study found that differences in weighted ICs that are well below observational uncertainty can lead to very different forecast outcomes. It was also discovered that while reducing the IC uncertainty can have a positive effect on the accuracy of a forecast, a bifurcation point, in some cases, can be reached at which point no further gains from reducing IC uncertainty can be made. It is unclear, however, as to whether their results are specific to the case studied or can be generalized to more MCS events.

Durran and Weyn (2016) generated a twenty-five-member numerical model ensemble to study the error growth dynamics and predictability for squall lines. They argue that the downscale error growth from the synoptic-scale is more important than the upscale growth from small-scale errors. The authors suggest that improving observations and data assimilation on the larger scale rather than the smaller scale may be more effective for improving forecasts exceeding lead times of 3-4 h. Lawson and Gallus (2016) further studied the predictability of bow echoes, a subset of squall lines. The authors utilized multiple ensemble prediction system configurations to study two bow echo cases and it was found that IC uncertainty and variability

had the most influence on MCS positioning while model error exerted the most control on storm mode.

Prior research has also been conducted on other MCV events. For example, a numerical ensemble forecast was utilized to analyze the dynamics of the long-lived MCV of 10-13 June 2003 (Hawblitzel et al. 2007). Ensemble results showed that MCV formation was more likely when mid-level cyclonic vorticity existed before MCS initiation. The study also discovered that convection played a significant role in intensifying the mid-level shortwave through diabatic heating as the increased upper-level latent heat release led to more upper-level potential vorticity. The amplified mid-level shortwave led to more convective development downstream and the formation of the MCV. The longevity and evolution of the MCV was controlled by the secondary convection it produced. Ensemble members that produced poor or fair simulations of the MCV also produced less secondary convection leading to much shorter or non-existent MCV longevity than well-performing ensemble members.

The objective of this research is to determine the predictability of the 8 May 2009 "Super Derecho." We want to determine if NWP models are capable of providing an accurate forecast of this and, by extension, other high impact MCS(s) a day in advance. This research would also add to the small amount of literature on MCS predictability. Learning more about the dynamics of warm-core mesovortex formation is another goal of this research as ensemble predictability studies can provide insight into what environments are more favorable for mesovortex formation. Hawblitzel et al. (2007) and Schumacher et al. (2013) found that an accurate CI forecast is important to the overall convective system evolution. A posterior hypothesis was created stating that initial convection must develop early enough in order for a strong circulation associated with the warm-core mesovortex to exist. CI is important because it allows the characteristic

airstreams of a mature MCS sufficient time prior to the observed mesovortex time to form, which Evans et al. (2014) found to be important for a circulation associated with the mesovortex to develop. We hypothesize that if CI does not occur early enough, the circulation associated with the mesovortex will be non-existent or weak. The experimental design is discussed in the following section. The third section contains the results and a discussion. Lastly, a summary is presented in the final section.

2. Methodology

a. Cycled Analysis

The WRF-ARW version 3.7.1 (Skamarock et al. 2008) is utilized to carry out the experiment. The Data Assimilation Research Testbed (DART, lanai release, rev. 8336; Andersen et al. 2009), as coupled with WRF-ARW version 3.7.1, is utilized to assimilate observations and generate ensemble ICs via an ensemble adjustment Kalman filter (EnKF; Anderson 2001). Cycled data assimilation begins at 1200 UTC 2 May 2009 and continues every six hours until 1200 UTC 7 May 2009, at which time 50-member ensemble forecasts (described below) are launched. Assimilation is conducted on a domain that is centered over the conterminous United States and extends into Canada, Mexico, and the Atlantic and Pacific Oceans (Fig. 1). It has 15-km horizontal grid spacing with 415 x 325 grid points and 50 vertical levels. Model parameterizations include: the Thompson microphysics scheme (Thompson et al. 2008), the Mellor-Yamada-Janjic (MYJ) planetary boundary layer (PBL) scheme (Janjic 1994), the Rapid Radiative Transfer Model for Global Climate Models (RRTMG) for both longwave and shortwave radiation (Iacono et al. 2008), the revised Tiedtke cumulus parameterization scheme (Tiedtke 1989; Zhang et al. 2011), and the NOAH land surface model (Chen and Dudhia 2001) (see Table 1). The Thompson microphysics scheme was chosen after Romine et al.

(2013), whose work has strong similarities in the environment and convective phenomena compared to ours, found that Thompson had reduced spurious precipitation rates compared to the Morrison microphysics scheme. Romine et al. (2013) also found that the Tiedtke cumulus parameterization scheme forecast lower tropospheric temperatures the closest to observations and that the MYJ PBL tends to have a cooler and moister boundary layer than the Yonsei University PBL scheme (Hong et al. 2006). To generate ICs, the 1200 UTC 2 May 2009 Global Forecast System (GFS) analysis is perturbed via 50 random samples of the National Center for Environmental Prediction (NCEP) background error covariance matrix (Barker et al. 2012). Lateral boundary conditions (LBCs) for each model advance during cycled data assimilation are provided by 0-h GFS analyses and 6-h GFS forecasts, as perturbed using the fixed covariance perturbation technique of Torn et al. (2006). Adaptive Gaspari-Cohn localization (Gaspari and Cohn 1999; Anderson 2012), sampling error correction (Anderson 2012), and time- and space-varying adaptive inflation are applied to the assimilation to decrease spurious correlations due to sampling errors and preserve ensemble spread (e.g., Torn 2010, Romine et al. 2013, Schwartz et al. 2014). See Table 2 for more information about the DART setup.

Multiple sources were employed for observation processing and quality control. Observations were gathered from standard aviation routine weather reports [METARs; *u, v, T,* altimeter (Alt)*,* specific humidity (SH)], Global Systems Division Meteorological Data Ingest System for mandatory level rawinsondes and dropsondes (*u, v, T,* Alt*,* SH), marine stations (*u, v, T,* Alt*,* SH), aircraft (ACARS; *u, v, T,* SH), profilers (*u, v,* pressure), atmospheric motion vectors (AMVs; *u, v*; Velden et al. 2005), and Global Positioning System (GPS) radio occultation refractivity (Kursinski et al. 1997). The AMVs were processed by and obtained from the Cooperative Institute for Satellite Studies Space Science and Engineering Center (CIMSS). The

GPS data was processed by and obtained from the Constellation Observing System for Meteorology Ionosphere and Climate. Table 3 provides a complete list of observations types, assumed observation errors, and observation windows and an example of a single observation assimilation cycle is provided in Fig. 2. Additionally, changes to surface observation errors following Ha and Snyder (2014) and middle troposphere rawinsonde wind errors following Romine et al. (2013, 2014) were made to improve assimilation quality. Finally, specific humidity errors follow Schwartz et al. (2015a). Model variables that were updated during cycled analysis include: U, V, W, T, T2, QVAPOR, Q2, QCLOUD, QRAIN, QNRAIN, QSNOW, QICE, QNICE, QGRAUP, H_DIABATIC, REFL_10CM, PH, MU, V10, U10, and PSFC. Soil state is updated with soil data from the GFS analyses after data assimilation but before the next cycle begins.

Extra observation processing included (i) observational error was increased within five grid points of the domain's lateral boundaries; (ii) surface observations were excluded when the station height and model terrain contrasted by more than 300 m; and (iii) the distance thresholds for aircraft and satellite-derived observations for wind were changed to ±22.5 km and ±25 hPa in the horizontal and vertical, respectively, to superob such observations that are densely packed following Ha and Snyder (2014).

Several studies have incorporated DART to generate numerical model ensembles for convection-permitting forecasts. Romine et al. (2013) compared the results of different physics suites to understand sensitivity to model bias in a continuously cycled ensemble data assimilation system. They found that observations and model parameterizations were sources of bias and that different physics parameterizations also had different biases. Romine et al. (2014) performed another experiment with WRF-ARW and DART to better ensemble forecast reliability. A WRF-

ARW 50-member EnKF via DART was also utilized to simulate convection-permitting forecasts to focus on hourly precipitation forecasts using both probabilistic and deterministic methods (Schwartz et al. 2014). It was determined that all ensemble members forecast too much precipitation but that the most skillful and valuable EnKF forecast guidance is given by probabilistic forecasts from the ensemble as a whole. Schwartz et al. (2015b) also conducted real-time convective-allowing ensemble forecasts utilizing the EnKF data assimilation system to study the ensemble's performance with respect to precipitation and severe weather guidance. They found that more skillful forecasts were obtained from 1200 UTC initializations rather than 12-hrs earlier at 0000 UTC and ensemble forecasts were more skillful than GFS-initialized forecasts. However, the 1200 UTC initializations contained a moist bias relative to the 0000 UTC initializations. Dual-resolution (DR) hybrid variational-ensembles were compared to their single-resolution (SR) counterparts for evaluating performance and 72-h WRF Model forecasts (Schwartz et al. 2015c). Overall, DR and SR analyses initialized forecasts were not statistically different suggesting a DR hybrid system could benefit ensemble forecasting. Torn and Romine (2015) utilized convection-allowing ensemble forecasts with an EnKF to examine upstream sub-synoptic forecast errors during the Mesoscale Predictability Experiment (MPEX). Probabilistic forecasts for a three-day period of heavy-rain produced by an MCS were investigated by coupling the EnKF with high-resolution WRF ensembles with mixed physics and varying assimilation methods. The ensemble forecasts were compared to the Center for the Analysis and Prediction of Storms real-time ensemble forecasts. The authors discovered that precipitation forecast variability for the period was affected by the placement of upstream mid-level potential vorticity anomalies.

b. Free Forecasts

Ensemble forecasts start at 1200 UTC 7 May 2009, run for thirty-six hours, and are conducted on a two-way nested domain. The outer domain is described in the previous section while the inner domain has 1580 x 1000 horizontal grid points with 3-km grid spacing and 50 vertical levels. It is centered inside the cycled analysis domain and covers the CONUS (Fig. 2). The results of this study focus exclusively on the inner domain. A 50-member ensemble forecast is conducted using ICs provided by coupling WRF-ARW with the EnKF implemented within DART, as described above. LBCs are provided every 3 h from the 1200 UTC 7 May 2009 forecast cycle of the NCEP GFS model. The 6-h GFS forecasts are linearly interpolated for the 3 h intervals and data for each interval are perturbed using the fixed covariance perturbation technique of Torn et al. (2006). The frequency of model output is hourly. Physical parameterizations employed by the ensemble forecasts are identical to those described for the cycled analysis system except that convection on the forecast domain is treated explicitly (without parameterization; see Table 1).

c. Ensemble Sensitivity Analysis

Results from the ensemble simulations are analyzed using the ensemble-based sensitivity analysis (ESA) of Ancell and Hakim (2007) and Torn and Hakim (2008). In this method, for a given ensemble size M, the sensitivity of the ensemble-mean value of a forecast metric J to a change in an analysis state variable x is determined by the covariance of J and x divided by the variance of x. The equation below denotes a linear regression between the forecast metric **J** and the analysis state variable **x**.

$$\frac{\partial J}{\partial x} = \frac{\mathrm{cov}(\mathbf{J},\mathbf{x})}{\mathrm{var}(\mathbf{x})} \tag{1}$$

The forecast metric **J** is a $1 \times M$ ensemble estimate and there are $N \times M$ ensemble estimates for any given state variable **x** where N is equal to the number of horizontal grid points. Both **J** and **x**

have their ensemble means removed. In addition, the right-hand side of (1) is multiplied by the standard deviation of **x**, such that a one standard deviation change in **x** is responsible for the calculated (shown in figures) change in **J**. Simplified further, we aim to examine how **J** responds at the chosen forecast lead time to changes in **x** at prior lead times.

For our research, the forecast metric **J** is the 850 hPa maximum circulation over a 1° by 1° area ($m^2\ s^{-1}$) associated with the warm-core mesovortex at 1200 UTC 8 May 2009. The sensitivity was tested for other hourly times from 1000-1400 UTC 8 May 2009 and it was found that ESA results were qualitatively similar. Thus, the results are considered to be robust and trustworthy. The simulated mesovortex is manually located for each ensemble member and then the coordinates for the chosen point are utilized to find the circulation's maximum value within a 1° latitude by 1° longitude box. This box is distinct from the box used to compute the 850 hPa maximum circulation described above. The maximum value for each ensemble member is then employed to compute the sensitivity metric from the time of forecast initiation to the chosen forecast hour (1200 UTC 8 May 2009).

ESA has been employed in previous studies dealing with deep convection. Weisman et al. (2015) utilized ESA during MPEX to show where targeted observations could lead to better representation of meteorological features. This, in turn, would hopefully lead to improved forecasts. For the 19 May 2013 severe weather event, ESA helped improve MPEX's real-time ensemble forecasts by displaying there was large forecast error associated with an upstream trough. Targeted dropsonde observations were released within this region of forecast error and helped numerical models better resolve the trough. The research by Torn and Romine (2015) mentioned above also utilized ESA with their WRF EnKF ensemble forecasts. Two events were studied: 19 May 2013 and 31 May 2013. The positioning of the upstream trough as well as

lower tropospheric baroclinic boundaries were deemed to be important for convection forecasts in both events. Additionally, a southern Plains severe convective event in April 2012 was examined employing ESA (Bednarczyk and Ancell 2015). ESA revealed that positional changes in the upper-level low and low-level thermodynamic features led to different evolutions for convection-permitting WRF forecasts.

d. Composites

To more easily compare synoptic and mesoscale environments between ensemble members with the strongest and weakest 850 hPa mesovortex circulations, six ensemble members with the strongest and weakest circulations from 1000 UTC to 1400 UTC on 8 May 2009 are utilized to create Strong (STRONG) and Weak (WEAK) composites, respectively. The time period from 1000 UTC to 1400 UTC of 8 May 2009 was the only subset considered, as this was the time when the observed and simulated mesovortices most rapidly intensified. Next, the ensemble mean and plus and minus one standard deviation of the circulation data were found. Ensemble members that were above (below) one standard deviation for at least two out of the five time steps were considered for STRONG (WEAK) and if there were more than six qualified members, the members with strongest (weakest) circulations were utilized for STRONG (WEAK). The Rapid Update Cycle (RUC) analysis (Benjamin et al. 2004) from 0600 UTC 8 May 2009 is employed as "truth" to compare the composites to the observed environment.

3. Results and Discussion

a. Data Assimilation Performance

Data assimilation performance was relatively consistent and well behaved throughout the cycled analysis. Twenty 6 h cycles were completed in order to allow for the development of flow-dependent forecast covariances, the adaptive inflation to settle down to a reasonable value,

and the model attractor to convert from the GFS (given that the 1200 UTC 2 May 2009 GFS analysis is utilized as the ICs) to the WRF-ARW. For all of the surface observation platforms, the root-mean-square-error (RMSE), total spread, and bias are reduced for the posterior compared to the prior at each analysis time (Fig. 3). The RMSE, total spread, and bias also do not amplify over time. The RMSE and total spread for a majority of the platforms are also nearly equal by the final cycled analysis time, which, from Houtekamer and Mitchell (1998) and Dowell et al. (2004), enables for reasonably accurate forecast error covariance statistics to be derived and used in the assimilation process. The performance is similar to NCAR's experimental convection-allowing ensemble (Schwartz et al. 2015), however somewhat contrary is METAR observations show that the total spread for observations of altimeter, u, and v is slightly higher than RMSE (Fig. 3c-e). This suggests that reducing the assumed observation errors may be beneficial for constraining the range provided by the ensemble to better match the uncertainty that exists due to error relative to the observations. A cool and slight moist bias is also evident (Fig. 3a-b), however they are out of phase temporally with each other. It is unclear whether these biases are reflective of the MYJ's well-known cool/moist bias in pre-convective boundary layers (e.g., Coniglio et al. 2013).

Vertical profile observation platforms show similar performance as the surface platforms and compare reasonably well with the real-time NCAR ensemble system (Figs. 4a-j). Most variables across the platforms have good agreement between RMSE and total spread, signifying well-tuned observation errors. However, the satellite AMVs (Fig. 4i-j) have a large total spread relative to RMSE. The assumed errors for the CIMSS AMVs in this research are greater than Romine et al. (2013, 2014) although assimilation is limited to CIMSS AMVs with a CIMSS quality control value of greater than three. This value is akin to the Romine et al. (2013, 2014)

standard. Thus, assimilation performance could be improved through improved internal specification of assumed AMV observation errors.

b. Ensemble Performance

Hourly 1-km above ground level (AGL) derived reflectivity was first plotted for all ensemble members as a preliminary assessment of the ensemble members' MCS evolution and intensity compared to the observed event. Each member attempts to produce a MCS in Kansas that travels eastward with time. However, the successfulness of the attempt for each member varies significantly. Plotted 1-km AGL derived reflectivity at 1200 UTC 8 May 2009 shows the vast spread between ensemble members 1-20 (Fig. 5). A few members (e.g., members 1, 10, 13, 16) appear to have a large, strong, and well-organized MCS while others (e.g., members 2, 5, 14, 17) are much less organized and weaker. The location of the MCSs between members also varies, as stronger members are generally poleward of the weaker members.

850 hPa circulation was then overlaid on the 1-km AGL derived reflectivity for each member. This variable was employed as a proxy for the warm-core mesovortex that was present in the observed event. The variable can be thought of as the area-averaged absolute vorticity, which has units of $\times 10^4$ s^{-1}. Fig. 6 displays that only a couple of members (1, 10, 13, 16) exhibit what appears to be akin to a strong mesovortex associated with the MCS. A time series of circulation for the 50-ensemble members displays the sensitive nature of this variable (Fig. 7) as every ensemble member's circulation exhibits different behaviors and strengths. The mean 850 hPa circulation was computed at each time step along with ±1 standard deviation from the mean. The hourly time series of the 850 hPa circulation from Evans et al. (2014) is also plotted for reference.

Weisman et al. (2013) identified through a surface analysis that the mesolow associated with the mesovortex had a pressure minimum 8 hPa lower than the environmental pressure. Mean sea-level pressure was analyzed hourly from 1100 UTC 8 May 2009 to 1700 UTC 8 May 2009 to determine if any ensemble members produced a pressure minimum that resembled the observed mesovortex. During this time period only seven out of fifty members produced a mesovortex pressure minimum 4 hPa lower than the environmental pressure at some point, with only one member exceeding the 8 hPa difference observed in Weisman et al. (2013). From these findings we ask the question: What synoptic and mesoscale differences between ensemble members lead to the different circulation behaviors and intensities? The following sections attempt to address this question.

c. Ensemble Sensitivity Analysis

From a synoptic-scale viewpoint, the 850 hPa circulation associated with the mesovortex at 1200 UTC 8 May 2009 is sensitive to the upstream 500 hPa trough around 6 h before 1200 UTC 8 May 2009 (Fig. 8). (This analysis is conducted at the 0600 UTC 8 May 2009 forecast time. Other forecast times surrounding 0600 UTC 8 May 2009 were analyzed and found to be qualitatively similar compared to any combination of forecast hours. Hours surrounding the chosen 850 hPa circulation time of 1200 UTC 8 May 2009 were also tested and found to be qualitatively similar.) A deeper trough is associated with a stronger 850 hPa circulation 6 h later. The 500 hPa cyclonic vorticity collocated with the trough is stronger, acting to increase the differential cyclonic vorticity advection over eastern Colorado and western Kansas. If a 500 hPa trough passes over a pre-existing baroclinic zone, the differential cyclonic vorticity advection creates or amplifies an existing area of surface low pressure. In our event, a warm front stretches east-northeast across southern Kansas from a surface low in the Texas Panhandle serving as the

pre-existing baroclinic zone. From the Pettersen-Sutcliffe development equation, increasing the magnitude of the 500 hPa cyclonic relative vorticity would generate greater differential cyclonic vorticity advection over the baroclinic zone creating a stronger surface low.

An amplified 500 hPa trough causes numerous altercations to the mesoscale environment. The 850 hPa meridional wind maximum, or low-level jet (LLJ), is strengthened in consequence of the stronger 850 hPa geopotential height gradient, which is caused by the stronger leeside cyclogenesis and downstream 850 hPa ridge. The LLJ, which stretches from western Texas into Kansas, is intensified and expanded into western and northern Oklahoma (Fig. 9). This should allow for greater 850 hPa moisture and thermal advection over the central Plains. Fig. 10 supports the idea of increased moisture advection, as a stronger circulation is associated with greater 850 hPa relative humidity in western and central Kansas. Likewise, a stronger circulation is associated with strengthened 850 hPa thermal advection where higher values of potential temperature are shifted northward into southern Kansas. The potential temperature gradient associated with the warm front is thus increased. We can reason that the previous two factors create a more favorable environment for deep, organized convection in western and central Kansas, as larger values of convective-available potential energy (CAPE) should be found farther north into this region. Indeed, the ESA agrees, as a stronger circulation is associated with larger values of MUCAPE in the southern half of Kansas 6 h before the reference time of 1200 UTC 8 May 2009 (Fig. 12).

Increased low-level convergence is found at the nose of the strengthened LLJ and should act to promote a packing of the isentropes at the LLJ's nose. In consequence, the LLJ ascends more rapidly assuming adiabatic flow. This strengthened ascent could aid CI. Our earlier hypothesis states that the timing of CI has a significant effect on the later strength of the 850 hPa

circulation associated with the mesovortex. This is examined more closely in the following subsection.

The strength of a front is determined by the magnitude of cross-frontal density gradient (Markowski and Richardson 2010). A larger packing of the isotherms across Kansas results in a stronger horizontal density gradient. The frontogenetic function states that a stronger horizontal density gradient results in a stronger frontal circulation:

$$F = \frac{\partial u}{\partial y}\frac{\partial \theta}{\partial x} + \frac{\partial v}{\partial y}\frac{\partial \theta}{\partial y} + \frac{\partial \omega}{\partial y}\frac{\partial \theta}{\partial z} - \frac{\partial}{\partial y}\left(\frac{q\theta}{c_p T}\right). \quad (2)$$

Thus, the magnitude of the wind shift across the front should be increased due to the more rapid change in horizontal density. Fig. 13 agrees and displays that decreased positive 850 hPa u winds in central and northern Kansas (north of the warm front) and increased positive 850 hPa u winds in southern Kansas and northern Oklahoma (south of the warm front) are associated with a stronger circulation. This regime acts to increase the cyclonic horizontal shear across the front and thus the cyclonic relative vorticity associated with the front. Weisman et al. (2013) noted that no appreciable background vertical vorticity existed prior to the MCS's formation but Evans et al. (2014) found that selected inflowing trajectories along the baroclinic zone did possess appreciable cyclonic vertical vorticity that could be subsequently amplified via system-scale stretching. In our research, increased cyclonic horizontal wind shear across the warm front is associated with a stronger circulation. Thus for ensemble members with a stronger circulation, more cyclonic relative vorticity exists in the background environment prior to MCS formation. It is hypothesized that the MCS airstreams would act to converge the cyclonic vertical vorticity as well as the vorticity contributions from the eddy and tilting terms of the local circulation tendency equation to create a local cyclonic vorticity maximum (i.e., the warm-core mesovortex; Evans et al. 2014).

d. Composites

STRONG and WEAK results shown in this section are all at 0600 UTC 8 May 2009 to support the ESA in the previous section. At 500 hPa, STRONG has a slightly more amplified trough (Fig. 14a) as the 5520 m geopotential height contour dips closer to the Montana/Wyoming border than in WEAK (Fig. 14b). The 0600 UTC 8 May 2009 RUC analysis displays a 500 hPa upstream trough that lies between the solutions of STRONG and WEAK.

As reasoned earlier, a more amplified 500 hPa trough would cause stronger leeside cyclogenesis along with an enhanced LLJ. In STRONG, the LLJ is more formidable and covers a larger region as 30 and 35 kt winds reach into southern Kansas and western Oklahoma, respectively (Fig. 16a). This corresponds very well against the RUC analysis (Fig. 17) with STRONG's LLJ only being marginally weaker and less expansive. Meanwhile, WEAK's LLJ does not stretch nearly as far poleward or eastward as southern Kansas and western Oklahoma have 5 and 15 kt lesser wind magnitudes, respectively, than STRONG (Fig. 16b). The enhanced LLJ in STRONG acts to advect more low-level moisture (Fig. 18a) evidenced by the 14°C isodrosotherm located in southwestern Kansas. The 14°C isodrosotherm in WEAK is lagging behind at the Kansas/Oklahoma border (Fig. 18b) contrasting significantly between STRONG (Fig. 18a) and the RUC analysis (Fig. 19).

Increased temperature advection is also noted in STRONG as the 22°C isotherm is situated in extreme southwestern Kansas (Fig. 18a) while WEAK's is still stretching through southeastern Colorado into the Oklahoma Panhandle (Fig. 18b). The temperature gradient is also greater across Kansas and the warm front is shifted northward in STRONG (Fig. 18a) compared to WEAK (Fig. 18b). The temperature gradient and placement of the warm front match very

closely in between STRONG and the RUC analysis (Fig. 19). As a result of the increased potential temperature gradient across the warm front, the amount of available instability across central Kansas is much more favorable for deep convection in STRONG (Fig. 20a) and the RUC analysis (Fig. 21) than WEAK (Fig. 20b). MUCAPE in excess of 1500 J/kg is over the southern half of Kansas in STRONG while WEAK's MUCAPE has been shunted to the south. Lesser most-unstable convective inhibition (MUCIN) is also present across central Kansas in STRONG (Fig. 20a) and observations (Fig. 21) relative to the WEAK (Fig. 20b) suggesting that WEAK's members will need stronger forced ascent in order to supply the necessary lift to generate new convection.

Plotted Q-vector convergence at 700 hPa displays a region of convergence, or forcing for upward vertical motion, in northwest Kansas for STRONG (Fig. 22a) relative to the surrounding region. WEAK, on the other hand, has a much weaker signal of forcing for upward vertical motion (Fig. 22b) in the same region. For STRONG members, CI occurred within the region of enhanced positive Q-vector convergence (Fig. 23) while WEAK's CI occurred 1-2 h later to the southeast in southern Kansas and northern Oklahoma (not shown). Western Kansas is where a significant difference in 850 hPa dewpoint temperature exists between the composites. It is believed that the increased moisture advection from the enhanced LLJ in STRONG allowed lifted elevated air parcels to reach their level of free convection and form the MCS's initial thunderstorms.

Vertical cross-sections were utilized to find the subtler differences between STRONG and WEAK that may have led to the contrast in CI. The cross-sections stretched meridionally from southwest Kansas to southwest Nebraska, from 900 hPa to 500 hPa in the vertical, and are averaged over ±5 grid points in the zonal direction. The cross-sections were similar to those

employed in Peters and Schumacher (2016) where they studied the upstream backbuilding of a simulated MCS. In STRONG, the aforementioned ascent is easily identified as the LLJ crosses over the frontal zone in central Kansas (Fig. 24a). Below 650 hPa towards the south (left side), the environment is characterized by large CAPE (in excess of 2000 J/kg) and CIN. There is also no strong lift in this region to overcome the negative buoyancy. However, in central Kansas a tongue of CAPE is located above 650 hPa within the region of isentropic ascent. Within and above this layer of positive buoyancy a region of high cloud-water mixing ratio exists signaling the presence of convection. This is the mean latitude of where CI occurs in STRONG members. WEAK, on the other hand, has nearly no CAPE located above 650 hPa within the region of isentropic ascent (Fig. 24b). Instead, CAPE is lagging to the south and is overall of less magnitude than STRONG. WEAK's isentropic ascent is also noticeably weaker as the strength of the LLJ has been decreased. As a result, convection is not present since there are no analyzed regions of high cloud-water mixing ratio.

The previous section demonstrated why CI occurred in STRONG members and not in WEAK members. CI may be crucial to mesovortex formation as it allows the characteristic airstreams of an MCS to develop, which will work to converge the background cyclonic absolute vorticity and form a mesovortex. All composite members' mesovortex circulations appear to obtain maximum intensity around 1200 UTC 8 May 2009 (Fig. 7). However, the intensity is much greater for STRONG members compared to WEAK. This suggests that the characteristic airstreams of the MCS in STRONG's members have more time to converge the cyclonic vertical vorticity as hypothesized in Evans et al. (2014). More background cyclonic absolute vorticity may also be present in STRONG members due to the enhanced warm front. Future work pertaining to the investigation of this subject is discussed in the closing section.

4. Summary and Future Work

This research examined the predictability and dynamics of the warm-core mesovortex associated with the 8 May 2009 "Super Derecho" event. The WRF-ARW numerical model was coupled with DART to create a 50-member convection-allowing ensemble. ESA was performed on the output to study what synoptic and mesoscale differences contributed to the varying strengths of the mesovortex. It was found that the strength of the upstream upper-level trough had an impact on the strength of the 850 hPa circulation associated with the mesovortex, with a more amplified trough being associated with a stronger circulation. The amplified trough had cascading effects on the mesoscale by enhancing the LLJ located over the Texas and Oklahoma Panhandles, the baroclinic zone situated over Kansas, and the amount of moisture advection into western Kansas. Six member composites of the strongest and weakest circulation members were analyzed and found to agree with the ESA results.

A circulation budget analysis (Davis and Galarneau 2009, Evans et al. 2014) for the ensemble member with the strongest (member 10) and weakest (member 5) 850 hPa circulations associated with the mesovortex will be the subject of future work. This will help test the hypothesis of CI needing to occur earlier in order to form a strong 850 hPa mesovortex associated circulation. Environmental differences, such as the amount of background cyclonic absolute vorticity, could also be drawn out of this analysis and used to argue in support of Weisman et al. (2013) or Evans et al. (2014).

The ensemble attempted to produce a convective feature that resembled a MCS via either isentropic ascent in northwest Kansas or the warm front near the Kansas/Oklahoma border in each of its members. However, only fourteen percent of the members produced a feature akin to the observed warm-core mesovortex. For this event and experimental setup, the predictability is

high for MCS formation regardless of whether members develop the MCS for the right reasons. However, the predictability is low for mesovortex formation. The low predictability displays the extreme sensitivity of mesovortex forecasts. The reduced spread and error in the posterior analysis at 1200 UTC 7 May 2009 gives a measure of the small variability across the ensemble ICs at the launch time of the free forecasts. Thus, seemingly miniscule IC errors could lead to either a successful or unsuccessful mesovortex forecast. The work of Hawblitzel et al. (2007) found similar results as the miniscule synoptic-scale initial perturbations used to generate their numerical ensemble led to some ensemble members having a MCV and some not. Additionally, they also found that the simulated MCV was sensitive to the intensity and evolution of the simulated convection. However, the MCV was, in part, influenced by the utilization of convective parameterization due to the relatively coarse grid spacing employed in their numerical model. Nonetheless, our results display a similar behavior as ensemble members that are able to develop initial convection earlier have a stronger mesovortex later.

Reducing the magnitude of forecast error would, in theory, lead to increased mesovortex predictability. However, as previously mentioned, Melhauser and Zhang (2012) found that a bifurcation point can be reached and no further reductions in forecast error will lead to forecast improvement. The bifurcation point in our research could very likely be a mesovortex or no mesovortex solution without any middle ground. Further study must also be conducted by testing the scales at which IC uncertainty is implemented and whether such a bifurcation point exists. Durran and Weyn (2016) showed that numerical forecasts could have more successful thunderstorm forecasts if the large-scale initial perturbations were reduced by a small amount, rather than employing larger reductions to smaller-scale perturbations. Would this hold true for a mesovortex, however? Our results displayed that the timing of CI appears to significantly

affect the development of the mesovortex. Thus, reducing the large-scale errors has the potential to improve the CI forecast and, in turn, possibly improve the mesovortex forecast. Numerical model performance with regard to CI has been the subject of many research papers (e.g., Lee et al. 1991; Wilson and Roberts 2006; Loftus et al. 2008; Duda and Gallus 2013; Kain et al. 2013; Burghardt et al. 2014).

The improvement in CI predictability still does not come without caveats with regards to the predictability for the formation of the mesovortex. Exponential error growth from deep, moist convection within the numerical models can have detrimental effects on forecasts. It could be very well likely that the limit of mesovortex predictability is also governed by model error. If this were the case, improvements in mesovortex predictability will require further advances in the physical parameterization packages that most directly influence convection initiation and evolution.

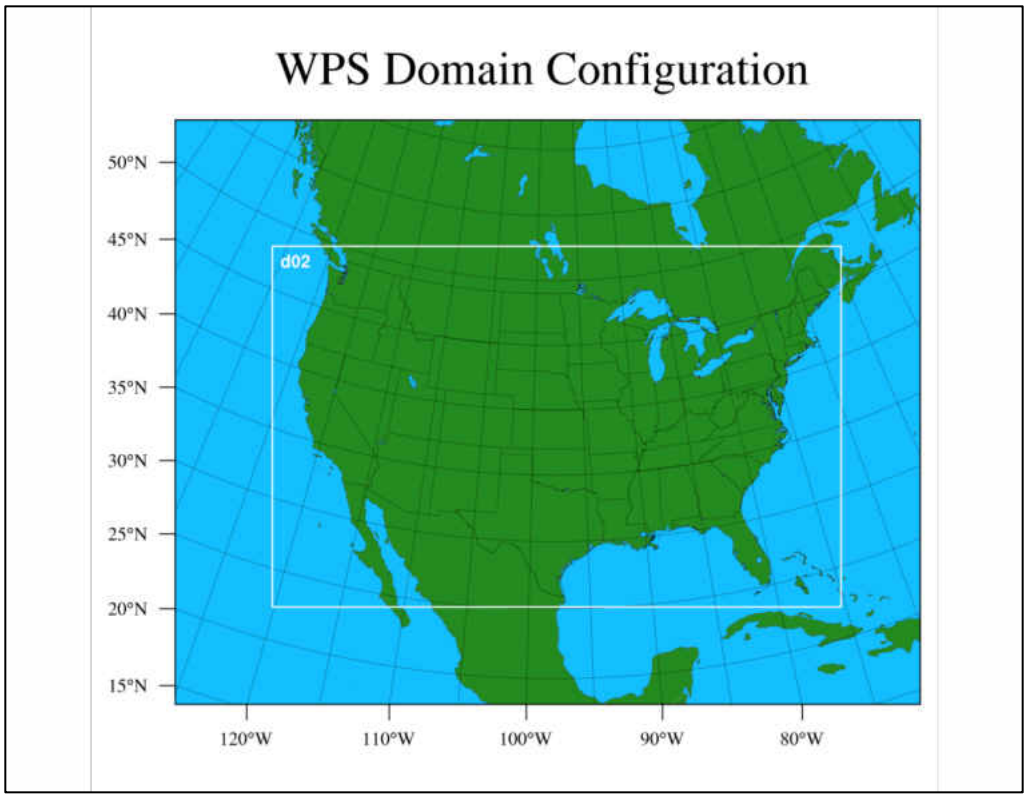

Figure 1: Domain configuration for the methodology. Cycled analysis is conducted on the outer domain while the free forecasts utilize both.

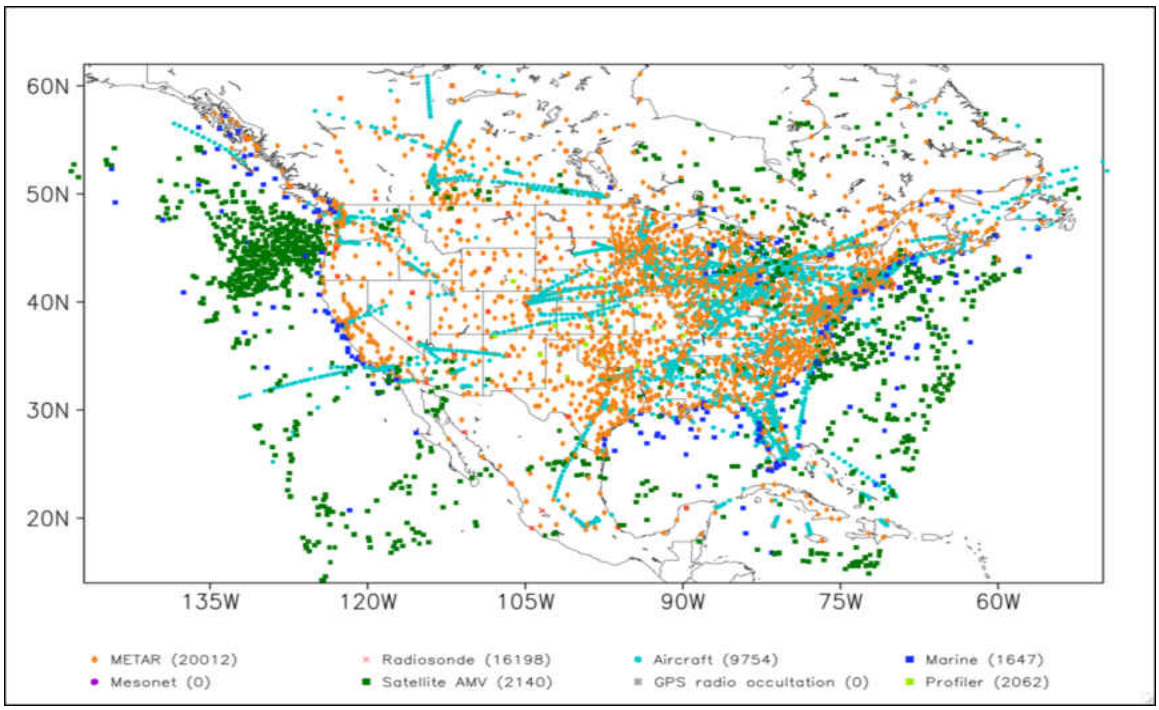

Figure 2: Spatial distribution of assimilated observation platforms for the 1200 UTC 7 May 2009 analysis cycle. Observation counts are for unique observations within each platform type.

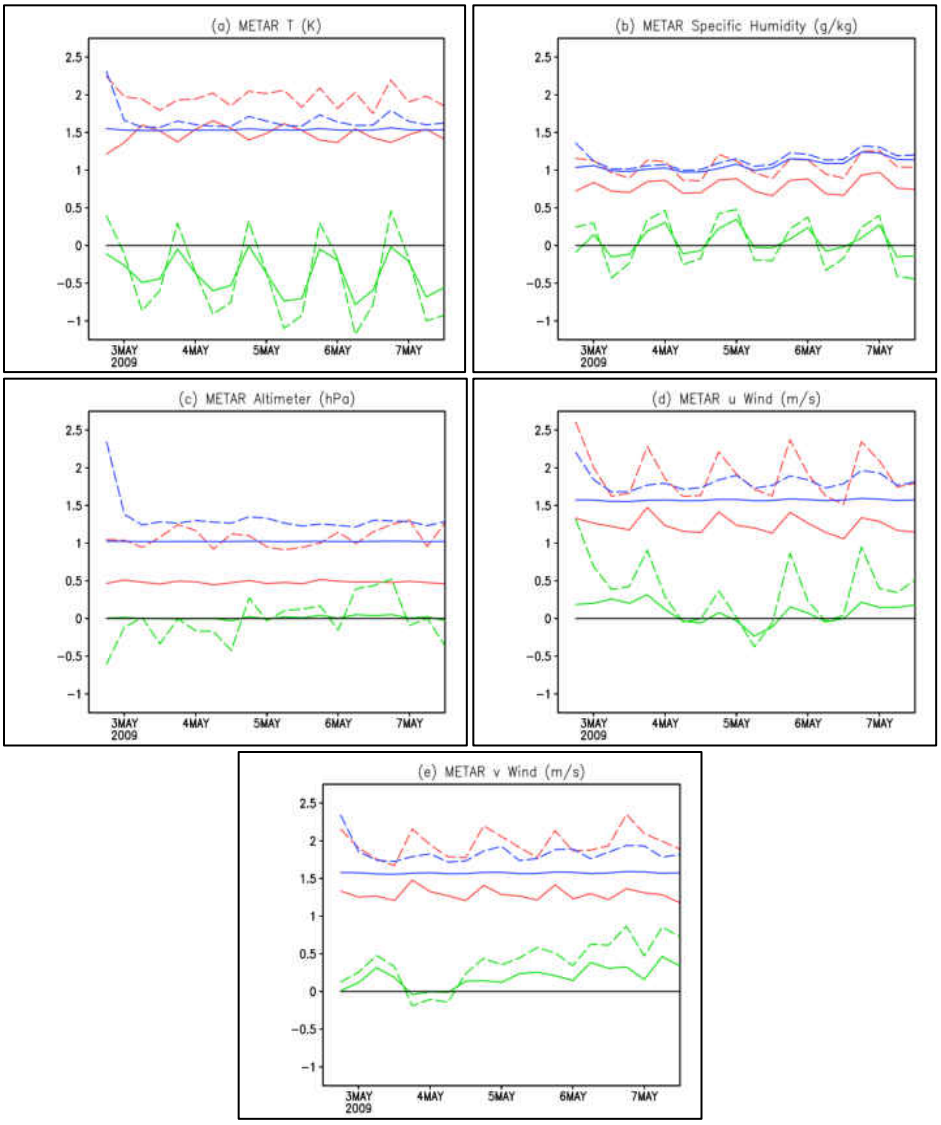

Figure 3: METAR (a) temperature (Kelvin), (b) specific humidity (g/kg), (c) altimeter (hPa), (d) *u* (m/s), and (e) *v* (m/s) assimilated observation statistics for 1200 UTC 2 May 2009 to 1200 UTC 7 May 2009. The dashed (solid) lines denote the prior (posterior) of the RMSE (red colored), total spread (blue colored), and bias (green colored).

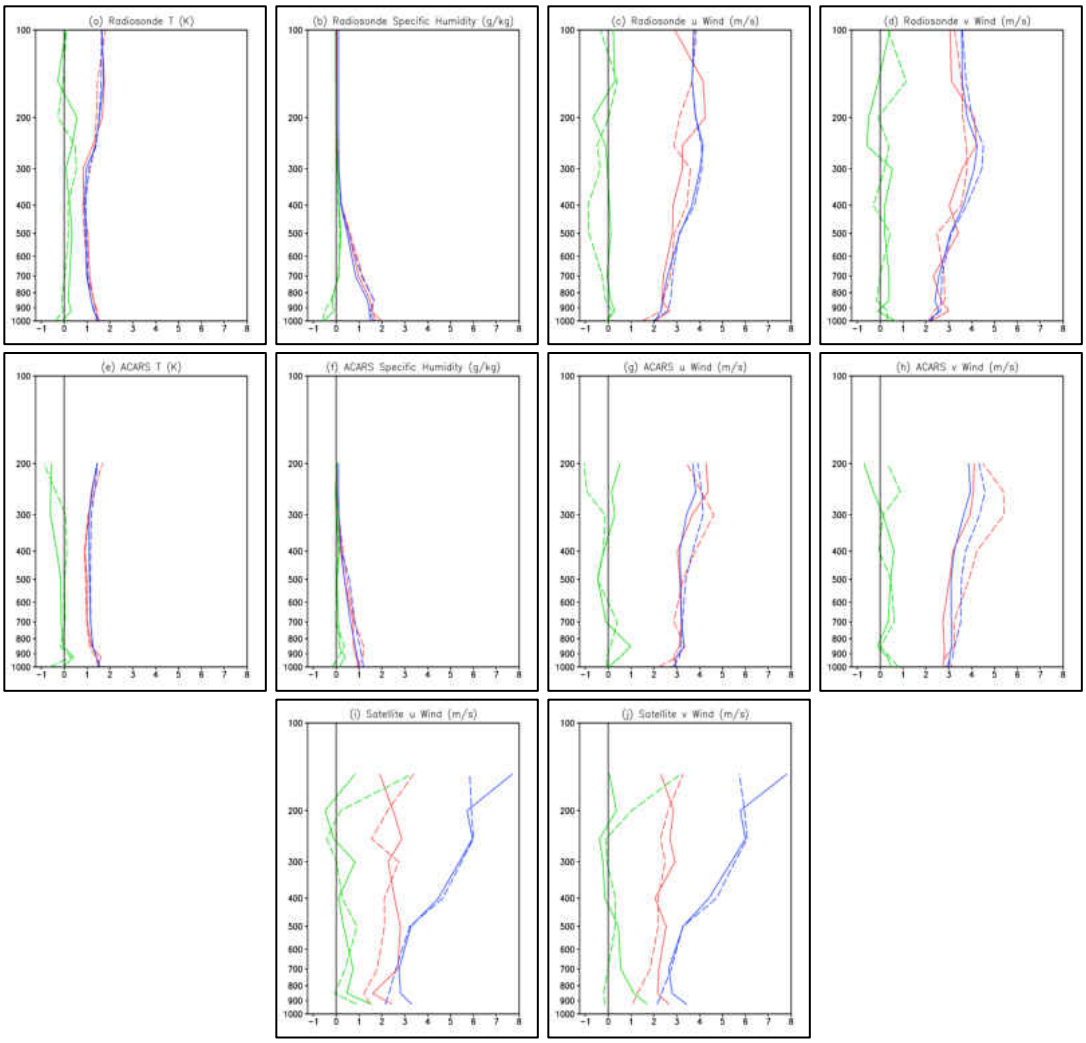

Figure 4: Assimilated observation statistics for: radiosonde (a) temperature (Kelvin), (b) specific humidity (g/kg), (c) *u* wind (m/s), and (d) *v* wind (m/s); ACARS (e) temperature (Kelvin), (f) specific humidity (g/kg), (g) *u* wind (m/s), and (h) *v* wind (m/s); and AMV (i) *u* wind (m/s), and (j) *v* wind (m/s). The solid (dashed) lines denote the 0000 UTC 5 May 2009 (1200 UTC 7 May 2009) time of the RMSE (red colored), total spread (blue colored), and bias (green colored).

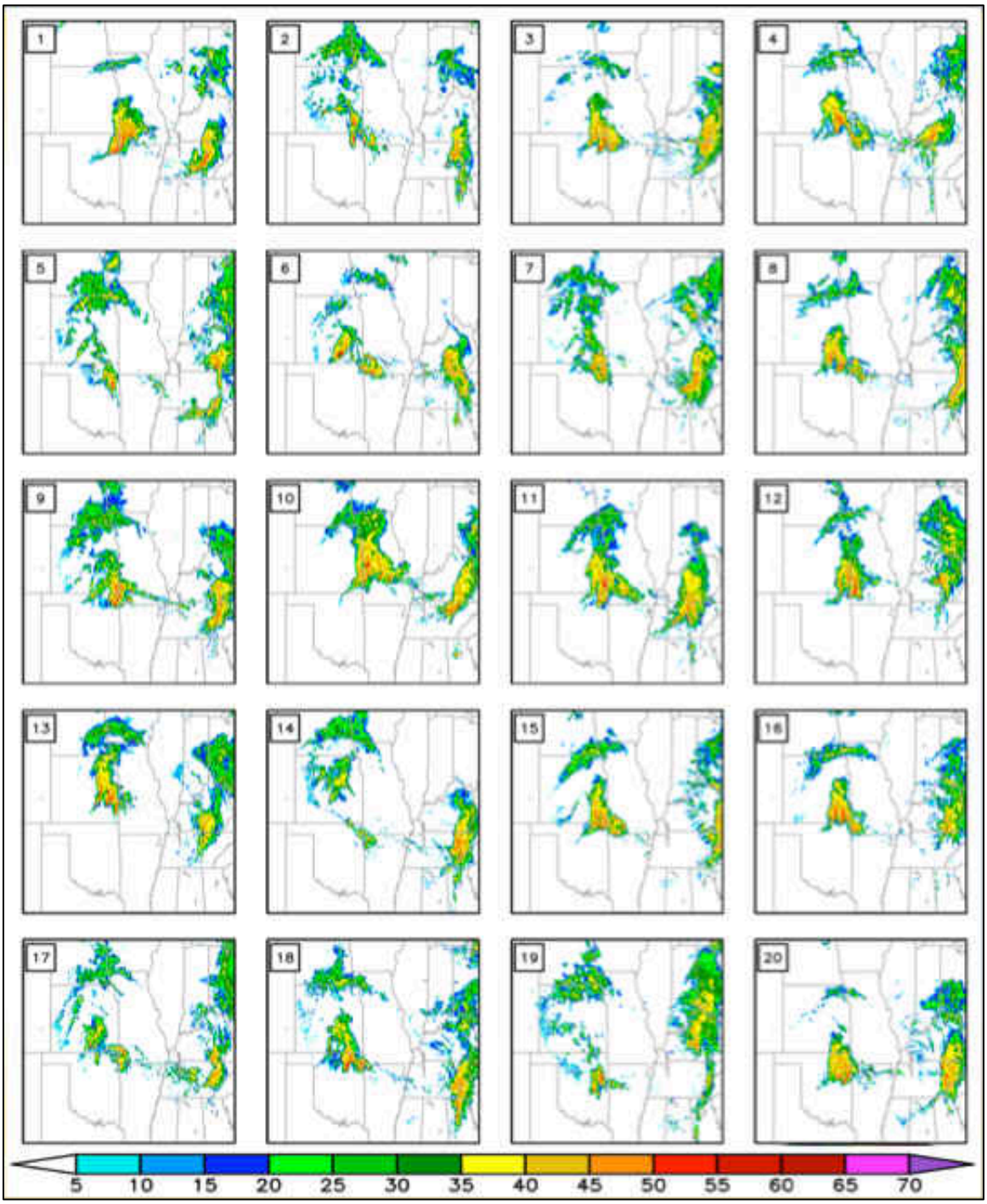

Figure 5: 1-km AGL derived reflectivity (dBZ) for ensemble members 1-20 at 1200 UTC 8 May 2009.

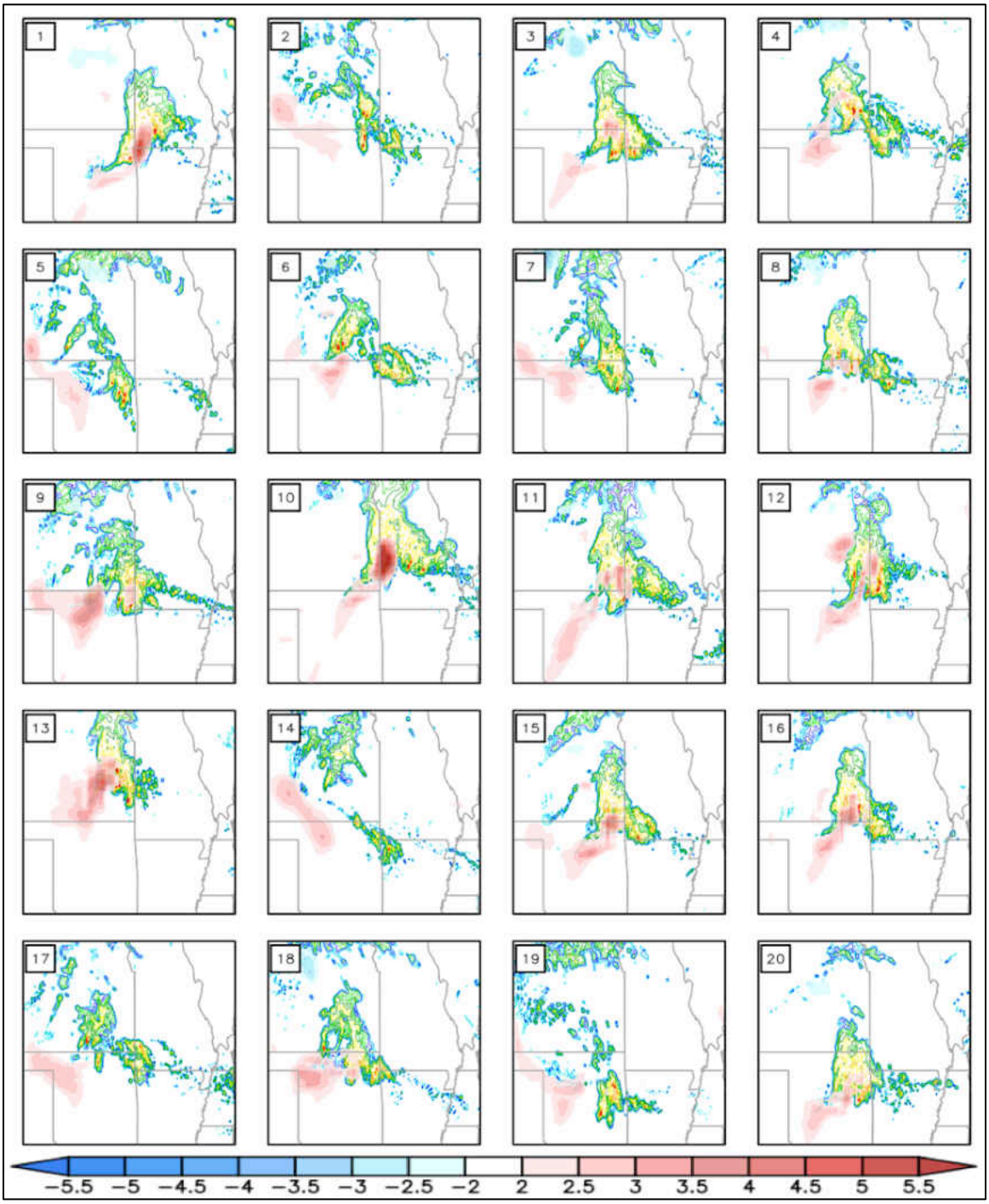

Figure 6: 850 hPa circulation calculated over a 1° by 1° box (color-shaded; $\times 10^6$ $m^2 s^{-1}$) overlaid on 1-km AGL derived reflectivity (color contoured; dBZ) for ensemble members 1-20 at 1200 UTC 8 May 2009.

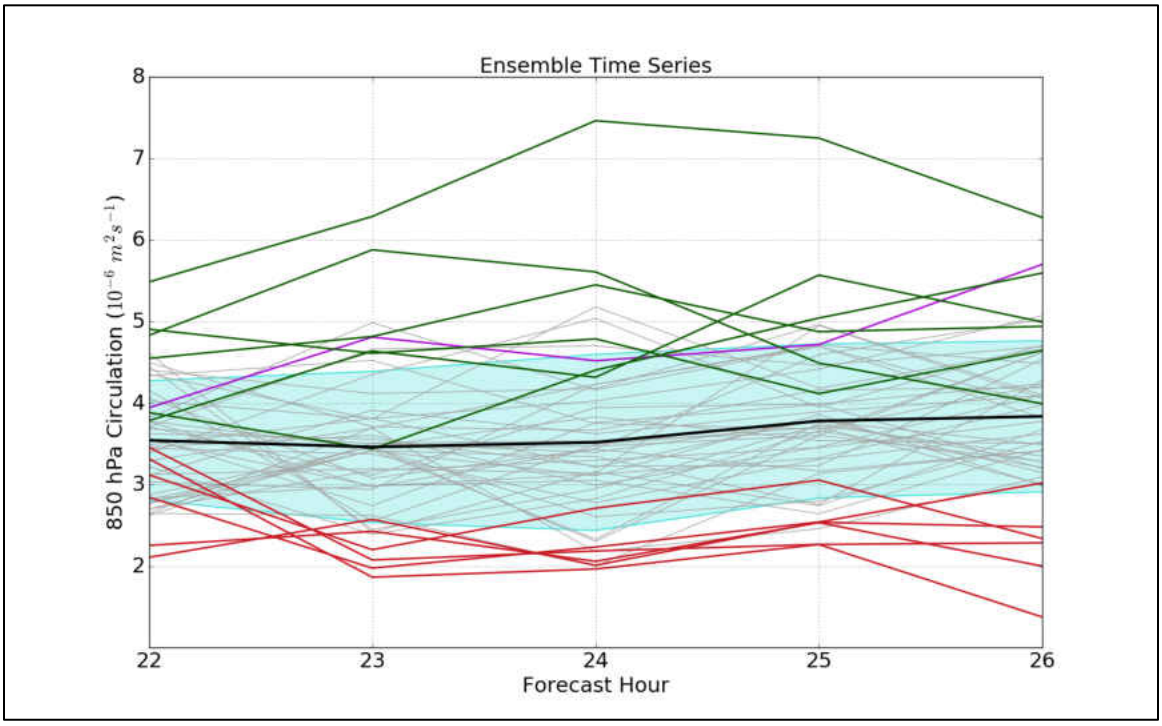

Figure 7: 850 hPa circulation (associated with the mesovortex) time series for the 50 ensemble members between 1000-1400 UTC 8 May 2009. The ensemble mean is denoted by the thick, black line, teal shading above (below) the ensemble mean denotes less than (greater than) one standard deviation above (below) the ensemble mean, Strong composite members (1, 10, 13, 15, 16, 26) are denoted by green lines, Weak composite members (5, 7, 18, 19, 28, 36) are denoted by red lines, all other members are denoted by grey lines, and the hourly time series of 850 hPa circulation from Evans et al. (2014) is denoted by the purple line.

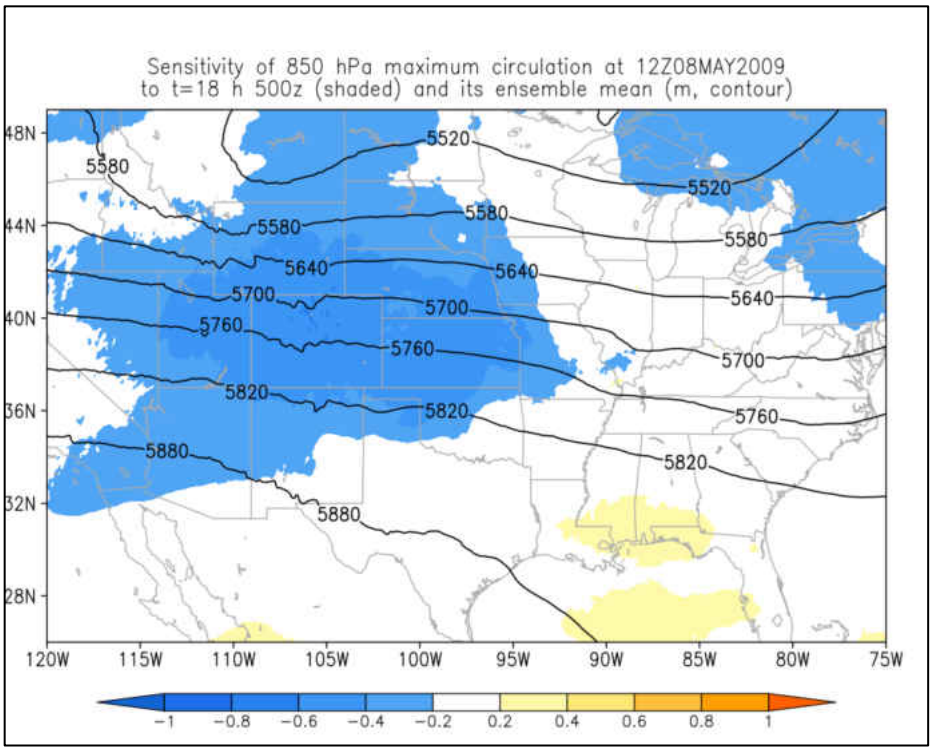

Figure 8: Ensemble sensitivity analysis for 500 hPa geopotential height (m) at 0600 UTC 8 May 2009 with respect to 850 hPa maximum circulation at 1200 UTC 8 May 2009. Black contours denote the ensemble mean while color-shading denotes the sensitivity metric $\frac{\partial J}{\partial x}$. Warm colors denote a positive relationship between **J** and **x** while cool colors denote a negative relationship between **J** and **x**.

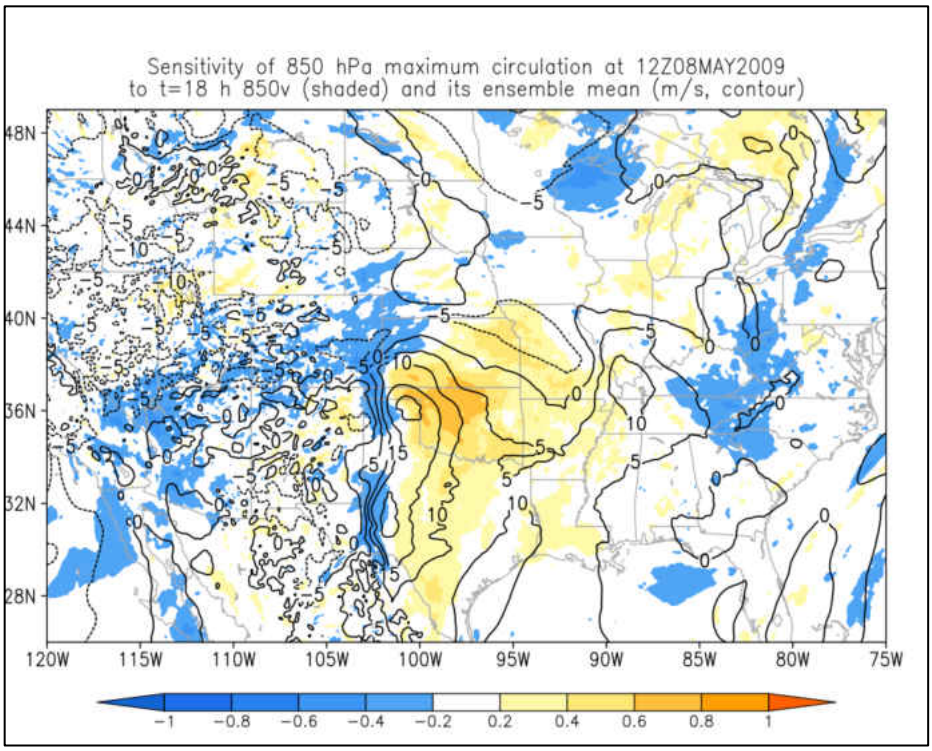

Figure 9: Same as Fig. 8 except the analysis state variable **x** is 850 hPa *v* wind (m/s) at 0600 UTC 8 May 2009.

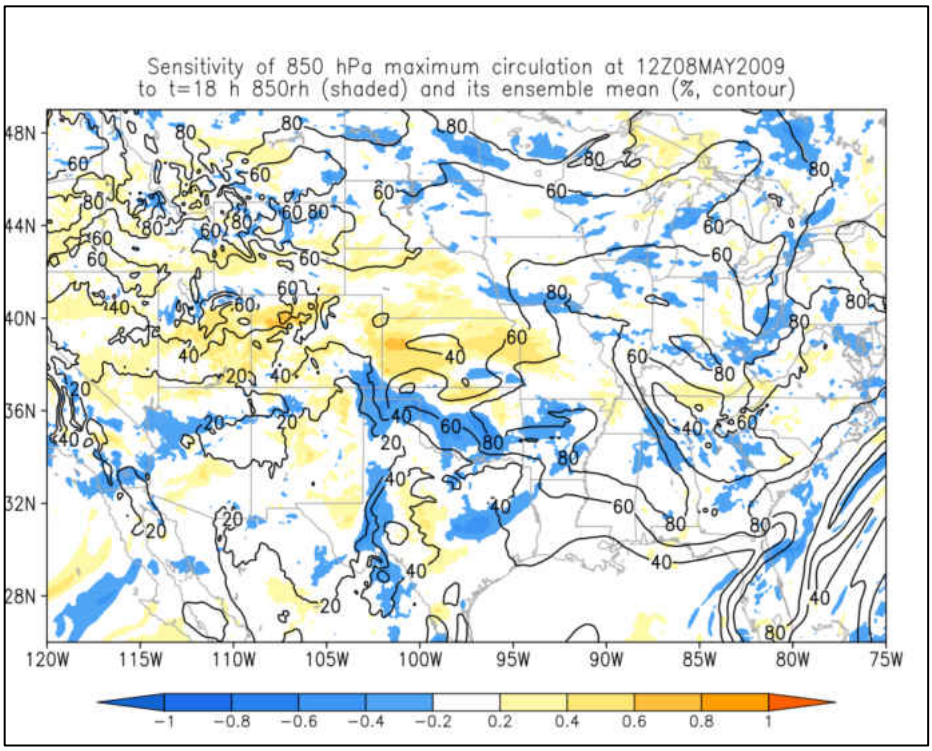

Figure 10: Same as Fig. 8 except the analysis state variable **x** is 850 hPa relative humidity (%) at 0600 UTC 8 May 2009.

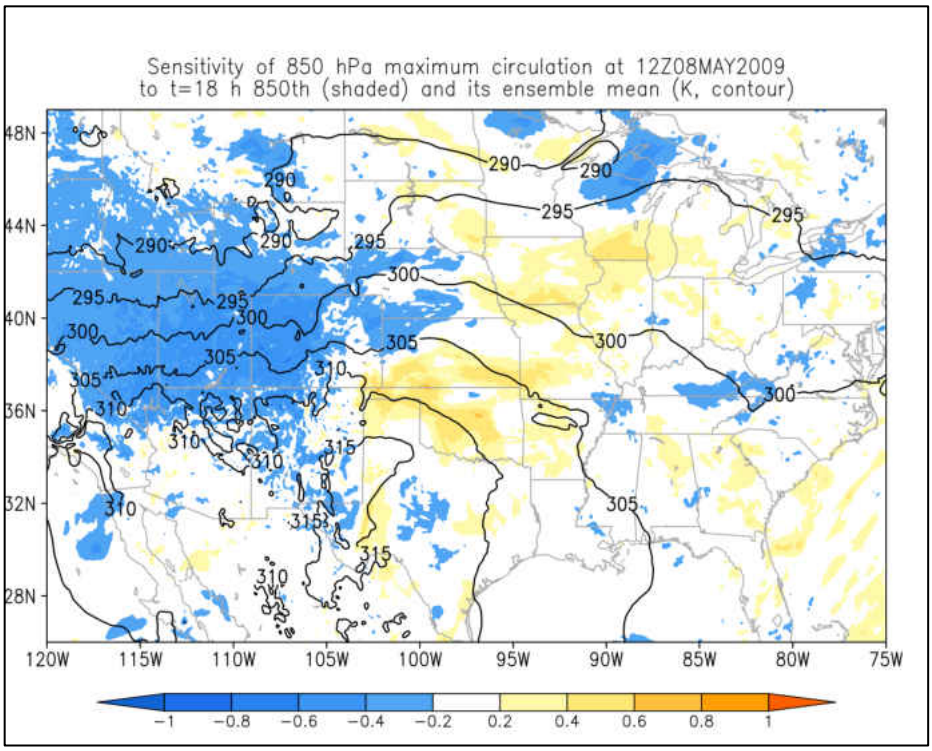

Figure 11: Same as Fig. 8 except the analysis state variable **x** is 850 hPa potential temperature (Kelvin) at 0600 UTC 8 May 2009.

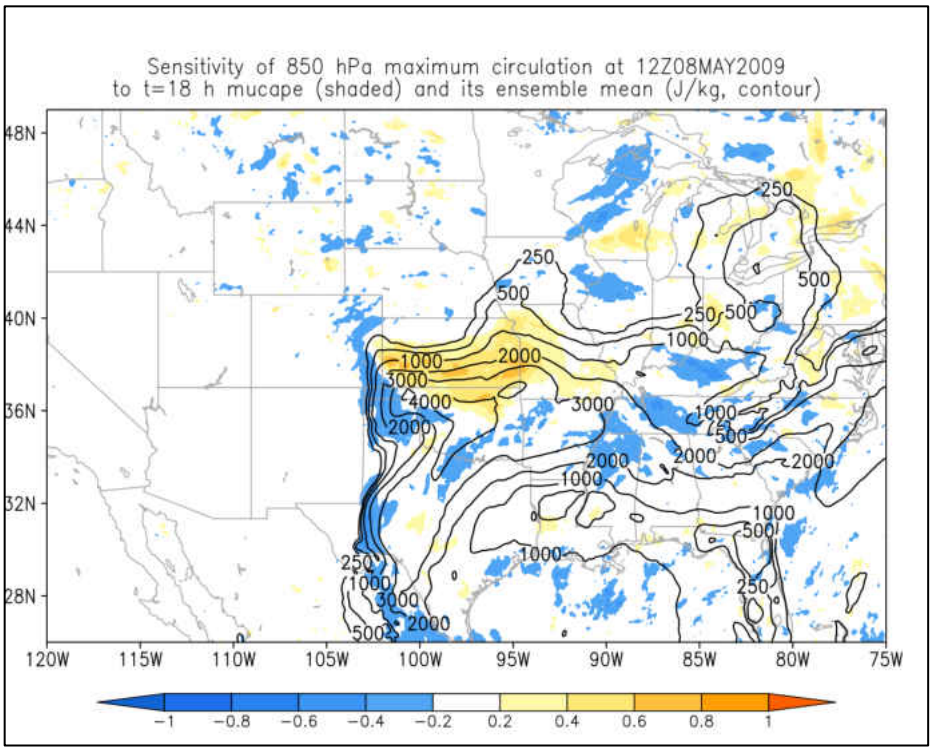

Figure 12: Same as Fig. 8 except the analysis state variable **x** is MUCAPE (J/kg) at 0600 UTC 8 May 2009.

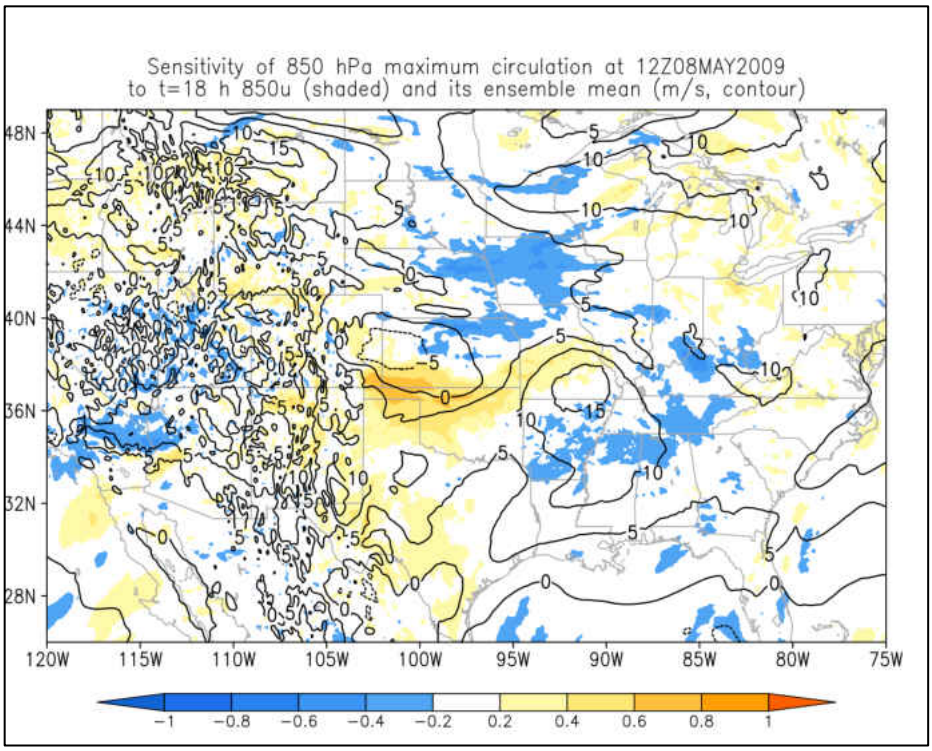

Figure 13: Same as Fig. 8 except the analysis state variable **x** is 850 hPa *u* wind (m/s) at 0600 UTC 8 May 2009.

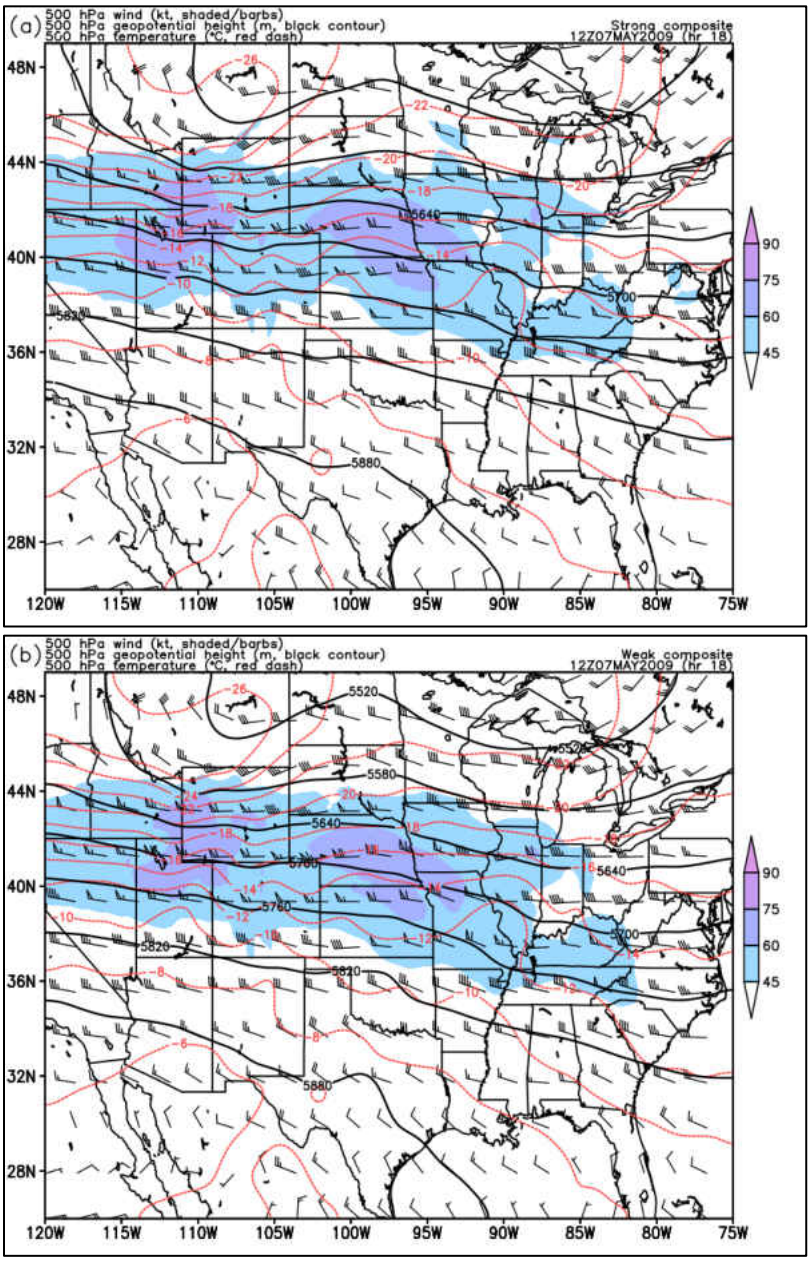

Figure 14: 500 hPa total wind (kt, color-shaded and barbs), 500 hPa geopotential height (m, black contours), and 500 hPa temperature (°C, red dashed) for (a) STRONG and (b) WEAK at 0600 UTC 8 May 2009.

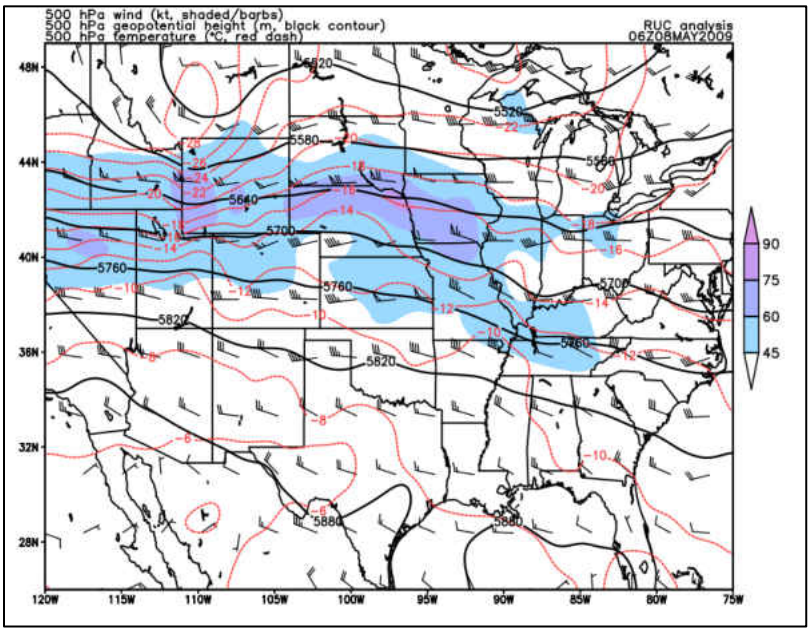

Figure 15: RUC analysis of 500 hPa total wind (kt, color shaded and barbs), 500 hPa geopotential height (m, black contours), and 500 hPa temperature (°C, red dashed) at 0600 UTC 8 May 2009.

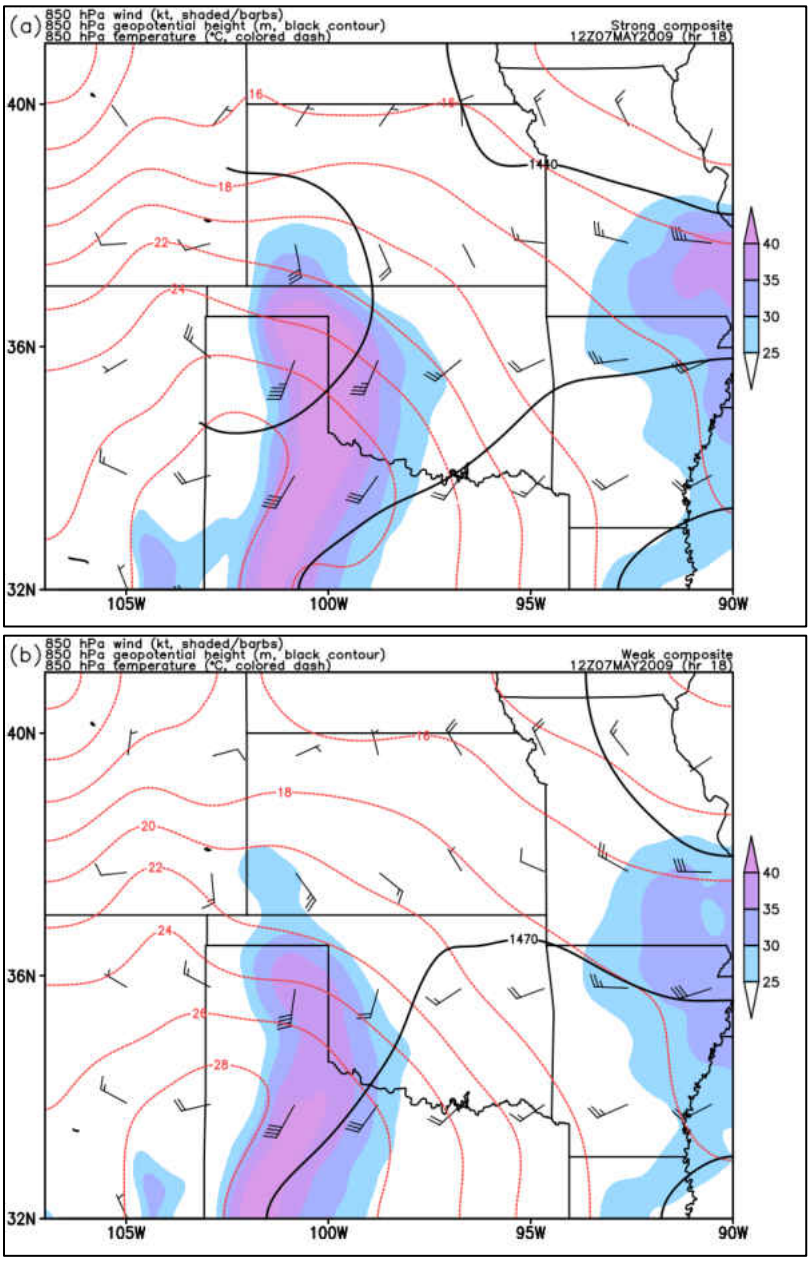

Figure 16: Same as Fig. 14 except for 850 hPa total wind (kt, color-shaded and barbs), 850 hPa geopotential height (m, black contours), and 850 hPa temperature (°C, red dashed).

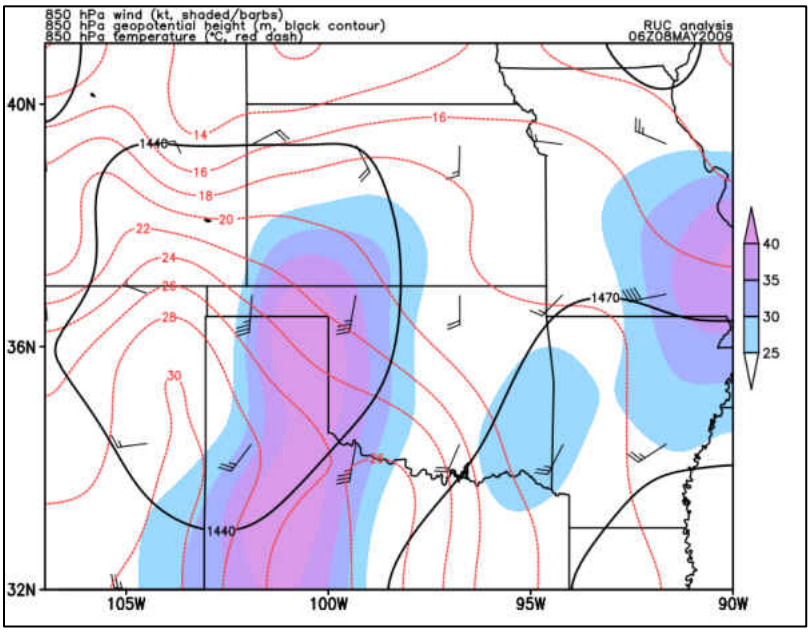

Figure 17: Same as Fig. 15 except for 850 hPa total wind (kt, color shaded and barbs), 850 geopotential height (m, black contours), and 850 hPa temperature (°C, red dashed).

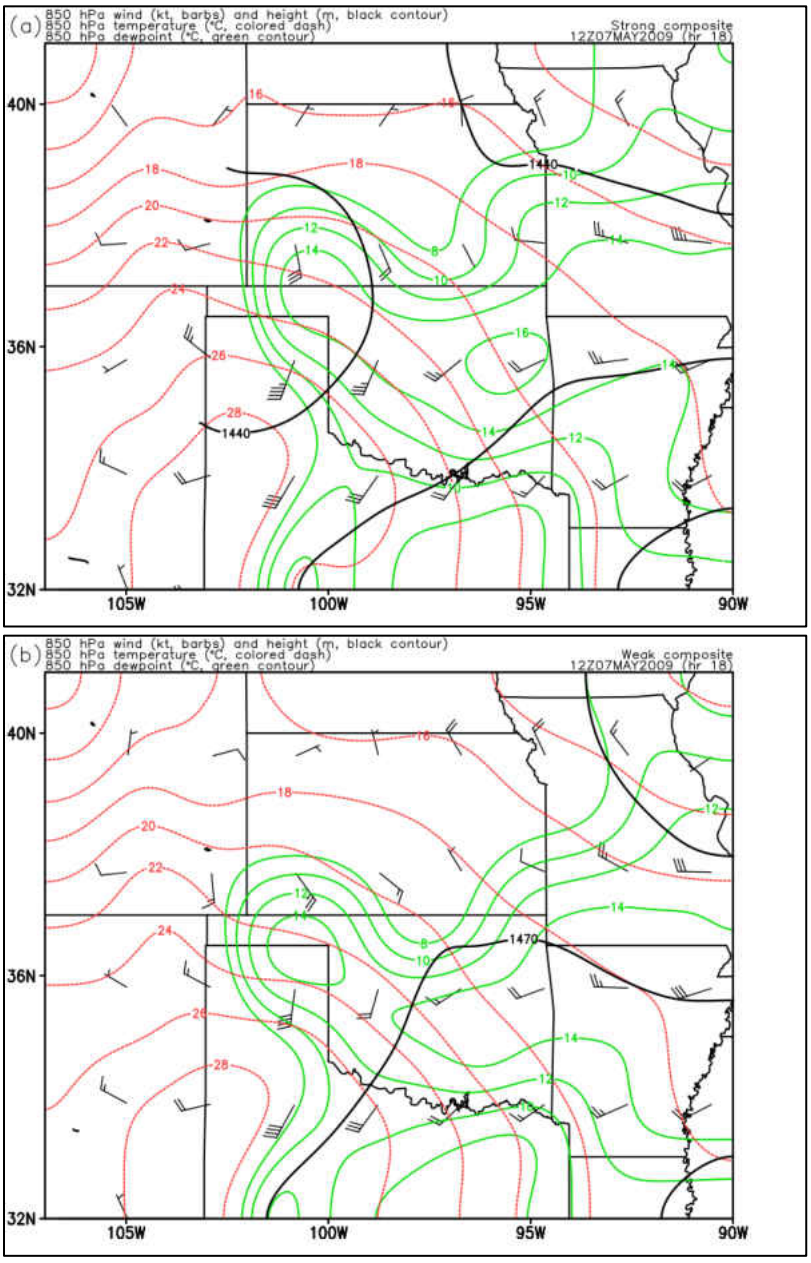

Figure 18: Same as Fig. 14 except for 850 hPa total wind (kt, barbs), 850 hPa geopotential height (m, black contours), temperature (°C, red dashed), and dewpoint (°C, green contours).

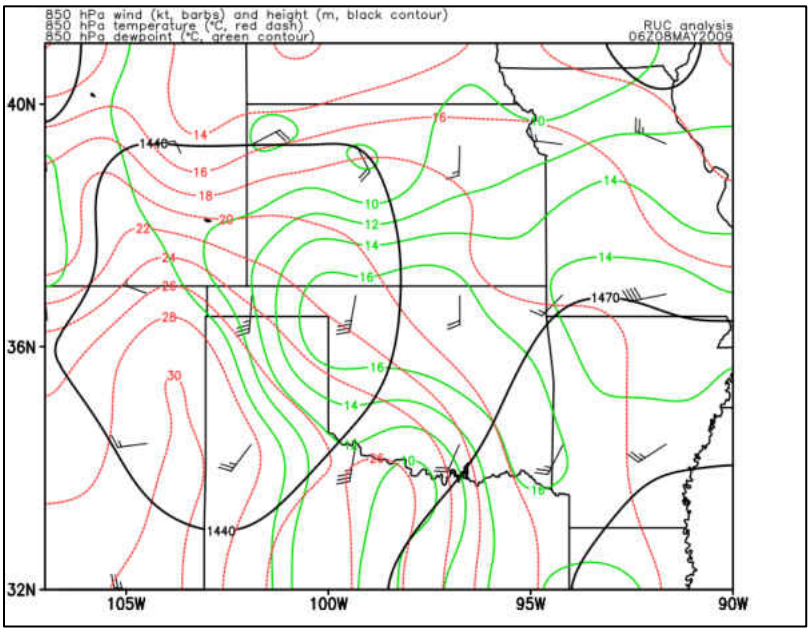

Figure 19: Same as Fig. 15 except for 850 hPa total wind (kt, barbs), 850 geopotential height (m, black contours), 850 hPa temperature (°C, red dashed), and 850 hPa dewpoint (°C, green contours).

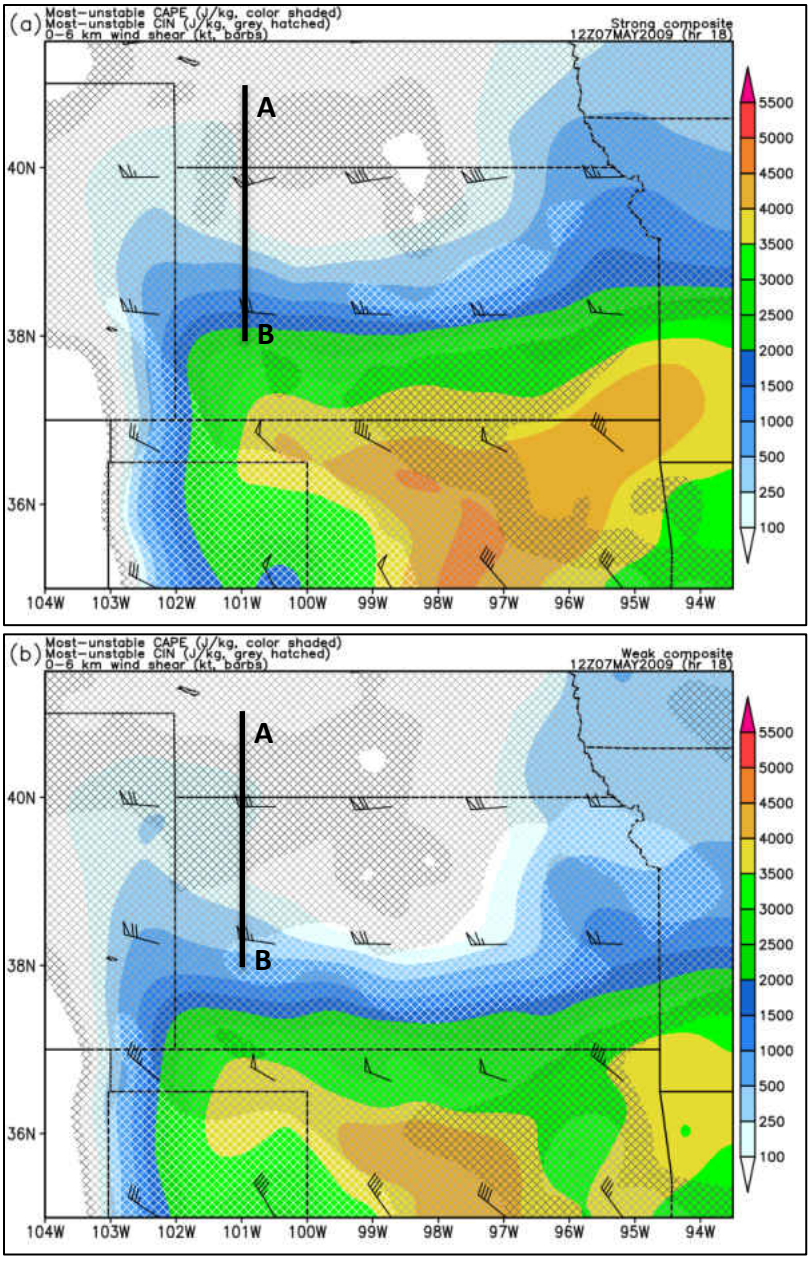

Figure 20: Same as Fig. 14 except for MUCAPE (J/kg, color shaded), MUCIN [J/kg, grey hatched (lighter colors denote greater values)], and 0-6 km wind shear (kt, barbs).

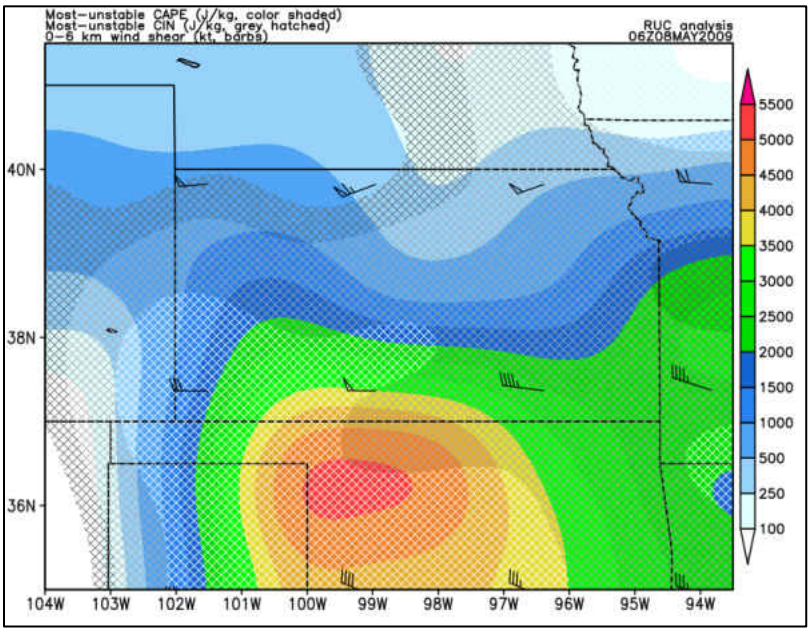

Figure 21: Same as Fig. 15 except for MUCAPE (J/kg, color shaded), MUCIN [J/kg, grey hatched (lighter colors denote greater values)], and 0-6 km wind shear (kt, barbs).

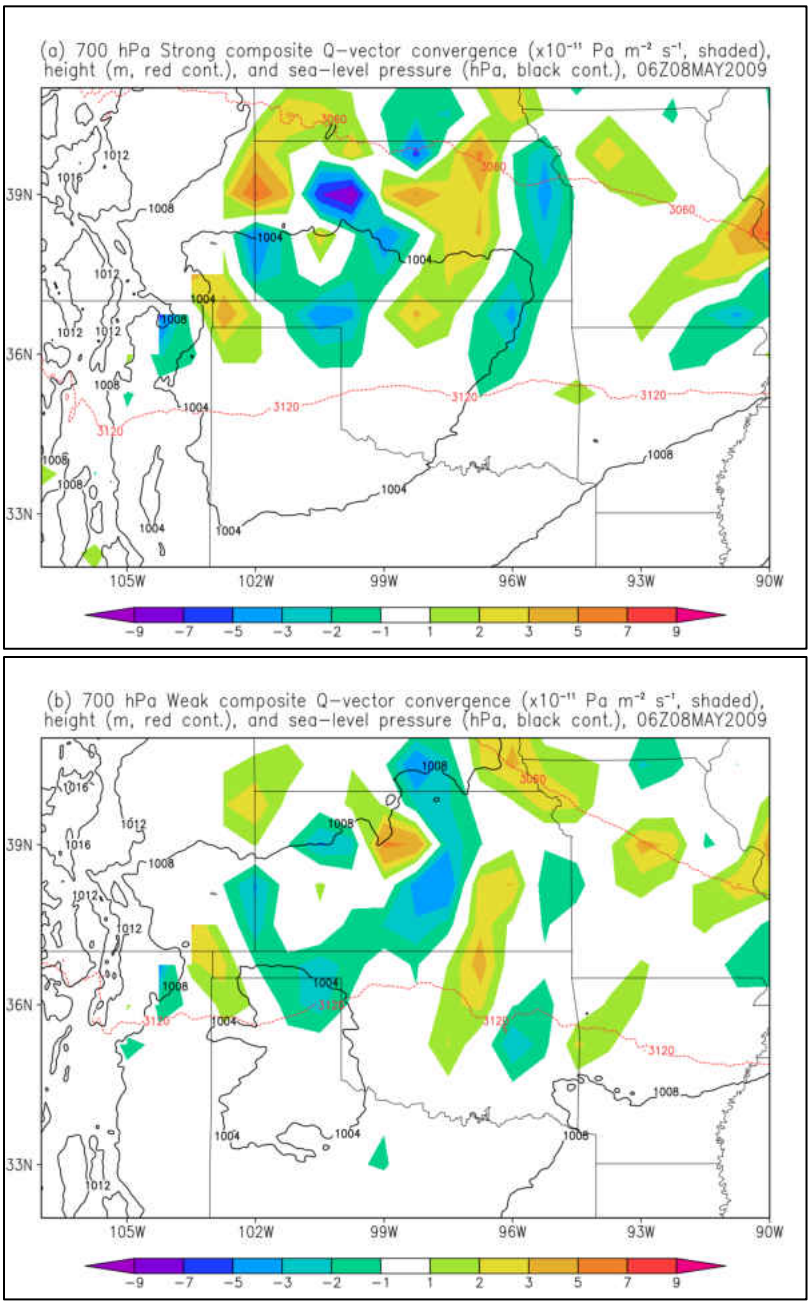

Figure 22: 700 hPa Q-vector convergence ($\times 10^{-11}$ m^{-2} s^{-1}, color shaded), 500 hPa geopotential height (m, red dashed), and sea-level pressure (hPa, black contour) for (a) STRONG and (b) WEAK at 0600 UTC 8 May 2009. Negative shaded values denote Q-vector convergence.

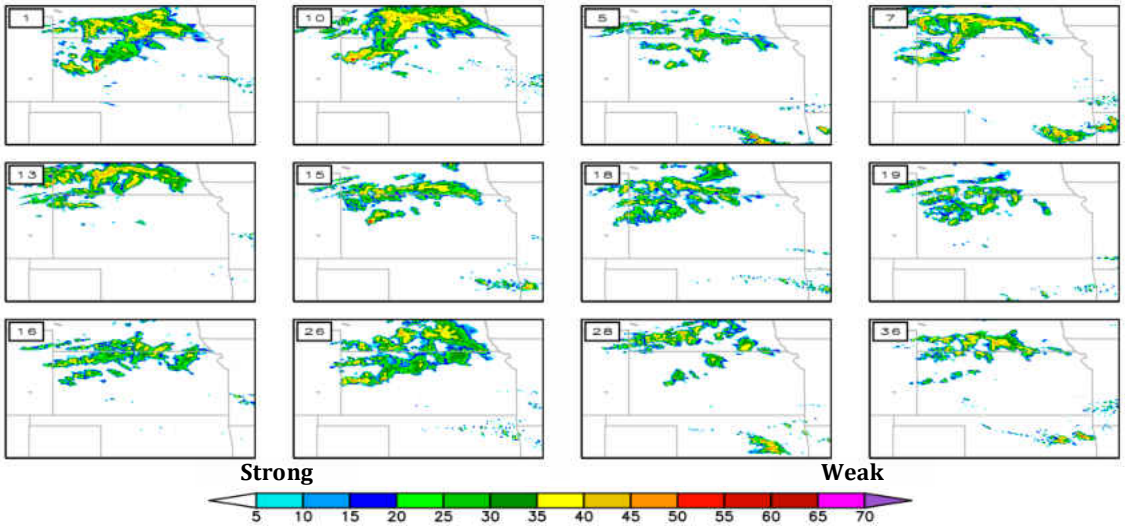

Figure 23: 1-km AGL derived reflectivity (dBZ) at 0600 UTC 8 May 2009 for each individual composite member. STRONG (WEAK) members are on the left (right) half.

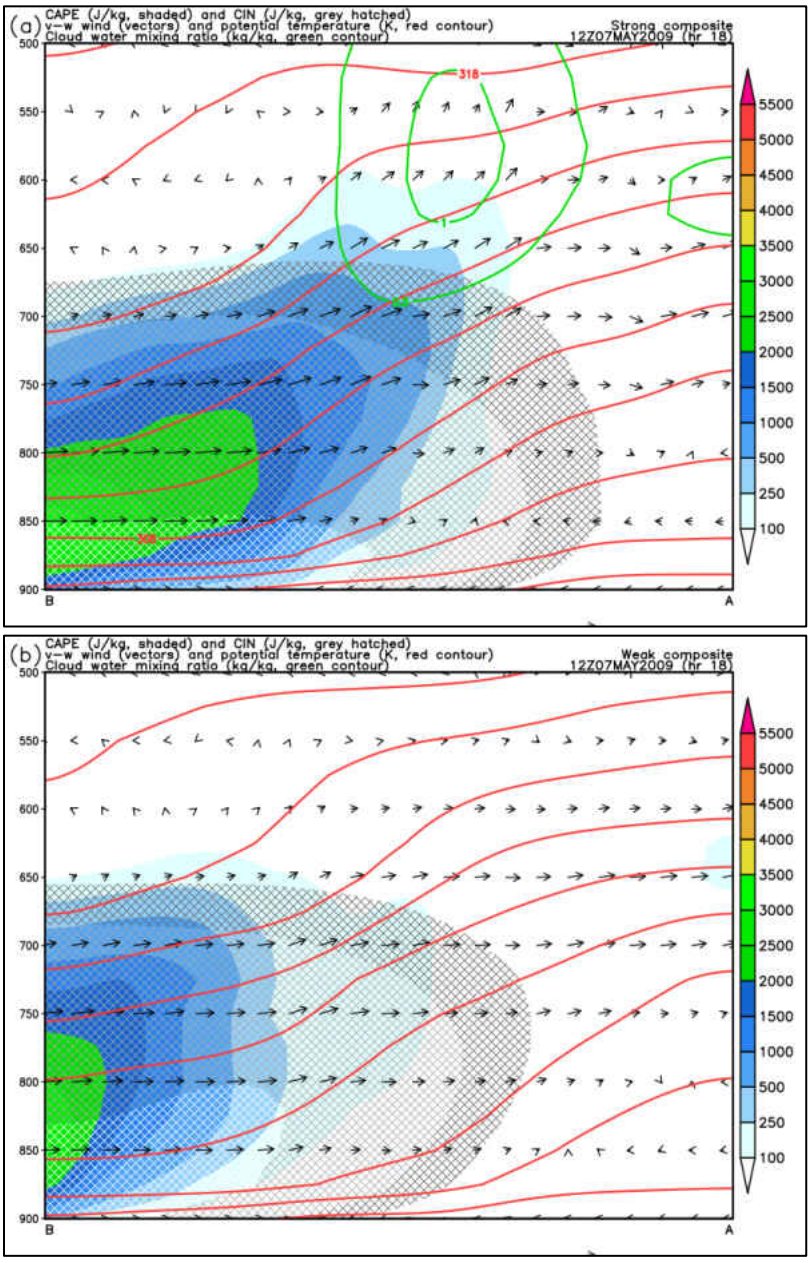

Figure 24: Plotted vertical cross-section of CAPE (J/kg, color-shaded), CIN [J/kg, grey hatched (lighter colors denote greater values)], *v*-*w* wind (m/s, vectors), isentropes (Kelvin, red contour), and cloud water mixing ratio (kg/kg, green contour) from A-B in Fig. 17 for (a) STRONG and (b) WEAK. The vertical axis is in units of hectopascals and the time is 0600 UTC 8 May 2009.

Parameter	Cycled Analysis	Free Forecasts
Horizontal Grid	415 x 325 Δx = 15 km	1581 x 1001 Δx = 3 km
Vertical Grid	50 levels p_{top} = 50 hPa	Same
Cumulus parameterization	New Tiedtke	None
Boundary layer parameterization	MYJ	Same
Microphysical parameterization	Thompson	Same
Longwave radiation	RRTMG	Same
Shortwave radiation	RRTMG	Same
Land-surface parameterization	NOAH	Same

Table 1: WRF model options.

Parameter	Value
Filter Type	Ensemble adjustment KF
Adaptive inflation	True—initial 1.0, 0.8 (mean, spread)
Adaptive localization threshold	2000
Localization type	Gaspari-Cohn
Horizontal localization half-width	635 km
Vertical localization half-width	8 km
Outlier threshold	3.0
Ensemble members	50
Sampling error correction	True
Assimilation interval	6 h

Table 2: DART options.

Platform	Variable	Observation Error	Observation Window
METAR	Temperature	Ha and Snyder (2014)	±1 hour
	E-W, N-S winds	Ha and Snyder (2014)	±1 hour
	Specific humidity	Schwartz et al. (2015a)	±1 hour
	Altimeter	NCEP statistics	±1 hour
Radiosonde	Temperature	Schwartz et al. (2015b)	±1 hour
	E-W, N-S winds	Romine et al. (2013, 2014)	±1 hour
	Specific humidity	Schwartz et al. (2015)	±1 hour
	Surface altimeter	NCEP statistics	±1 hour
Dropsonde	Temperature	NCEP statistics	±1 hour
	E-W, N-S winds	NCEP statistics	±1 hour
	Specific humidity	NCEP statistics	±1 hour
	Surface altimeter	NCEP statistics	±1 hour
Marine	Temperature	NCEP statistics	±1 hour
	E-W, N-S winds	NCEP statistics	±1 hour
	Specific humidity	Schwartz et al. (2015a)	±1 hour
	Altimeter	NCEP statistics	±1 hour
ACARS (22.5 km, 25 hPa)*	Temperature	NCEP statistics	±1 hour
	E-W, N-S winds	NCEP statistics	±1 hour
	Specific humidity	Schwartz et al. (2015a)	±1 hour
Profiler	E-W, N-S winds	NCEP statistics	±1 hour
	Pressure	NCEP statistics	±1 hour
Sat. Derived (22.5 km, 25 hPa)*	E-W, N-S winds	Romine et al. (2013)	±1 hour
GPS	RO refractivity	Kuo et al. (2004)	±1 hour

* Superobs (horizontal, vertical).

Table 3: Assimilated observation types, assumed observation errors, and observation windows.

References

Ancell, B., and G. J. Hakim, 2007: Comparing adjoint- and ensemble-sensitivity analysis with applications to observation targeting. *Mon. Wea. Rev.*, **135,** 4117-4134.

Anderson, J. L., 2012: Localization and sampling error correction in ensemble Kalman filter data assimilation. *Mon. Wea. Rev.*, **140,** 2359-2371.

--, T. Hoar, K. Raeder, H. Liu, N. Collins, R. Torn, and A. Avellano, 2009: The Data Assimilation Research Testbed: a community facility. *Bull. Amer. Meteor. Soc.*, **90,** 1283-1296.

--, 2001: An ensemble adjustment Kalman filter for data assimilation. *Mon. Wea. Rev.*, **129,** 2884-2903.

Barker, D. M., and Coauthors, 2012: The Weather Research and Forecasting model's community variational/ensemble data assimilation system: WRFDA. *Bull. Amer. Meteor. Soc.*, **93,** 831-843.

Bednarczyk, C. N., and B. C. Ancell, 2015: Ensemble sensitivity analysis applied to a Southern Plains convective event. *Mon. Wea. Rev.*, **143,** 230-249.

Benjamin, S. G., and Coauthors, 2004: An hourly assimilation-forecast cycle: The RUC. *Mon. Wea. Rev.*, **132,** 495-518.

Burghardt, B. J., C. Evans, and P. J. Roebber, 2014: Assessing the predictability of convection initiation in the High Plains using an object-based approach. *Wea. Forecasting*, **29,** 403-418.

Chen, F., and J. Dudhia, 2001: Coupling an advanced land surface-hydrology model with the Penn State-NCAR MM5 modeling system. Part I: Model implementation and sensitivity. *Mon. Wea. Rev.*, **129,** 569-585.

Coniglio, M. C., J. Correia, Jr., P. T. Marsh, and F. Kong, 2013: Verification of convection-allowing WRF model forecasts of the planetary boundary layer using sounding observations. *Wea. Forecasting*, **28,** 842-862.

--, S. F. Corfidi, and J. S. Kain, 2011: Environment and early evolution of the 8 May 2009 derecho-producing convective system. *Mon. Wea. Rev.*, **139,** 1083-1102.

--, J. Y. Hwang, and D. J. Stensrud, 2010: Environmental factors in the upscale growth and longevity of MCSs derived from Rapid Update Cycle analyses. *Mon. Wea. Rev.*, **138,** 3514-3539.

--, D. J. Stensrud, and M. B. Richman, 2004: An observational study of derecho-producing convective systems. *Wea. Forecasting*, **19,** 320-337.

Davis, C. A., and T. J. Galarneau, Jr., 2009: The vertical structure of mesoscale convective vortices. *J. Atmos. Sci.*, **66,** 686-704.

Dowell, D. C., F. Zhang, L. J. Wicker, C. Snyder, and N. A. Crook, 2004: Wind and temperature retrievals in the 17 May 1981 Arcadia, Oklahoma, supercell: Ensemble Kalman filter experiments. *Mon. Wea. Rev.*, **132,** 1982-2005.

Duda, J. D., and W. A. Gallus, Jr., 2013: The impact of large-scale forcing on skill of simulated convective initiation and upscale evolution with convection-allowing grid spacings in the WRF. *Wea. Forecasting*, **28,** 994-1018.

Dudhia, J., 1989: Numerical study of convection observed during the Winter Monsoon Experiment using a mesoscale two-dimensional model. *J. Atmos. Sci.*, **46,** 3077-3107.

Durran, D. R. and J. A. Weyn, 2016: Thunderstorms do not get butterflies. *Bull. Amer. Meteor. Soc.*, **97,** 237-243.

Evans, C., M. L. Weisman, and L. F. Bosart, 2013: Development of an intense, warm-core mesoscale vortex associated with the 8 May 2009 “super derecho” convective event. *J. Atmos. Sci.*, **71,** 1218-1240.

Gaspari, G., and S. E. Cohn, 1999: Construction of correlation functions in two and three dimensions. *Quart. J. Roy. Meteor. Soc.*, **125,** 723-757.

Ha, S.-Y., and C. Snyder, 2014: Influence of surface observations in mesoscale data assimilation using an ensemble Kalman filter. *Mon. Wea. Rev.*, **142,** 1489-1508.

Hawblitzel, D. P., F. Zhang, Z. Meng, and C. A. Davis, 2007: Probabilistic evaluation of the dynamics and predictability of the mesoscale convective vortex of 10-13 June 2003. *Mon. Wea. Rev.*, **135,** 1544-1563.

Hong, S.-Y., Y. Noh, and J. Dudhia, 2006: A new vertical diffusion package with an explicit treatment of entrainment processes. *Mon. Wea. Rev.*, **134,** 2318-2341.

Iacono, M. J., J. S. Delamere, E. J. Mlawer, M. W. Shephard, S. A. Clough, and W. D. Collins, 2008: Radiative forcing by long-lived greenhouse gases: Calculations with the AER radiative transfer models. *J. Geophys. Res.*, **113,** D13103.

Janjic, Z. I., 1994: The stop-mountain eta coordinate model: Further developments of the convection, viscous sublayer, and turbulence closure schemes. *Mon. Wea. Rev.*, **122,** 927-945.

Johns, R. H., and C. A. Doswell, III, 1992: Severe local storms forecasting. *Wea. Forecasting*, **7,** 588-612.

Kain, J. S., and Coauthors, 2013: A feasibility study for probabilistic convection initiation forecasts based on explicit numerical guidance. *Bull. Amer. Meteor. Soc.*, **94,** 1213-1225.

Kuo, Y.-H., T.-K. Wee, S. Sokolovskiy, C. Rocken, W. Schreiner, D. Hunt, and R. A. Anthes, 2004: Inversion and error estimation of GPS radio occultation data. *J. Meteor. Soc. Japan*, **82,** 507-531.

Kursinski, E. R., G. A. Hajj, J. T. Shofield, R. P. Linfied, and K. R. Hardy, 1997: Observing Earth's atmosphere with radio occultation measurements using the Global Positioning System. *J. Geophys. Res.*, **102** (D19), 23 429-23 465.

Lawson, J., and W. A. Gallus, Jr., 2016: On contrasting ensemble simulations of two Great Plains bow echoes. *Wea. Forecasting*. [Available online at journals.ametsoc.org/doi/10.1175/WAF-D-15-0060.1.]

Lee, B. D., R. D. Farley, and M. R. Hjelmfelt, 1991: A numerical case study of convection initiation along colliding convergence boundaries in northeast Colorado. *J. Atmos. Sci.*, **48,** 2350-2366.

Loftus, A. M., D. B. Weber, and C. A. Doswell, III, 2008: Parameterized mesoscale forcing mechanisms for initiating numerically simulated isolated multicellular convection. *Mon. Wea. Rev.*, **136,** 2408-2421.

Markowski, P. M., and Y. Richardson, 2010: *Mesoscale Meteorology in Midlatitudes*. Wiley-Blackwell, 407 pp.

Melhauser, C., and F. Zhang, 2012: Practical and intrinsic predictability of severe and convective weather at the mesoscales. *J. Atmos. Sci.*, **69,** 3350-3371.

Peters, J. M., and R. S. Schumacher, 2016: Dynamics governing a simulated mesoscale convective system with a training convective line. *J. Atmos. Sci.* [Available online at journals.ametsoc.org/doi/abs/10.1175/JAS-D-15-0199.1.]

Romine, G. S., C. S. Schwartz, C. Snyder, J. L. Anderson, and M. L. Weisman, 2013: Model bias in a continuously cycled assimilation system and its influence on convection-permitting forecasts. *Mon. Wea. Rev.*, **141,** 1263-1284.

--, --, J. Berner, K. R. Fossell, C. Snyder, J. L. Anderson, and M. L. Weisman, 2014: Representing forecast error in a convection-permitting ensemble system. *Mon. Wea. Rev.*, **142,** 4519-4541.

Schumacher, R. S., and A. J. Clark, 2014: Evaluation of ensemble configurations for the analysis and prediction of heavy-rain-producing mesoscale convective systems. *Mon. Wea. Rev.*, **142,** 4108-4138.

--, --, M. Xue, and F. Kong, 2013: Factors influencing the development and maintenance of nocturnal heavy-rain-producing convective systems in a storm-scale ensemble. *Mon. Wea. Rev.*, **141,** 2778-2801.

Schwartz, C. S., G. S. Romine, R. A. Sobash, K. R. Fossell, and M. L. Weisman, 2015a: NCAR's experimental real-time convection-allowing ensemble prediction system. *Wea. Forecasting*, **30,** 1645-1654.

--, --, M. L. Weisman, R. A. Sobash, K. R. Fossell, K. W. Manning, and S. B. Trier, 2015b: A real-time convection-allowing ensemble prediction system initialized by mesoscale ensemble Kalman filter analysis. *Wea. Forecasting*, **30,** 1158-1181.

--, Z. Liu, and X.-Y. Huang, 2015c: Sensitivity of limited-area hybrid variational-ensemble analyses and forecasts to ensemble perturbation resolution. *Mon. Wea. Rev.*, **143,** 3454-3477.

--, --, K. R. Smith, and M. L. Weisman, 2014: Characterizing and optimizing precipitation forecasts from a convection-permitting ensemble initialized by a mesoscale ensemble Kalman filter. *Wea. Forecasting*, **29,** 1295-1318.

Skamarock, W. C., and Coauthors, 2008: A description of the Advanced Research WRF version 3. NCAR Tech. Note NCAR/TN-475+STR, 113 pp. [Available online at http://www.mmm.ucar.edu/wrf/users/docs/arw_v3.pdf.]

Snively, D. V., and W. A. Gallus, Jr., 2014: Prediction of convective morphology in near-cloud-permitting WRF model simulations. *Wea. Forecasting*, **29,** 130-149.

Thompson, G., P. R. Field, R. M. Rasmussen, and W. D. Hall, 2008: Explicit forecasts of winter precipitation using an improved bulk microphysics scheme. Part II: Implementation of a new snow parameterization. *Mon. Wea. Rev.*, **136,** 5095-5115.

Torn, R. D., and G. S. Romine, 2015: Sensitivity of central Oklahoma convection forecasts to upstream potential vorticity anomalies during two strongly forced cases during MPEX. *Mon. Wea. Rev.*, **143,** 4064-4087.

--, 2010: Performance of a mesoscale ensemble Kalman filter (EnKF) during the NOAA high-resolution hurricane test. *Mon. Wea. Rev.*, **138,** 4375-4392.

--, and G. J. Hakim, 2008: Ensemble-based sensitivity analysis. *Mon. Wea. Rev.*, **136,** 663-677.

--, --, and C. Snyder, 2006: Boundary conditions for limited-area ensemble Kalman filters. *Mon. Wea. Rev.*, **134,** 2490-2502.

Tiedtke, M., 1989: A comprehensive mass flux scheme for cumulus parameterization in large-scale models. *Mon. Wea. Rev.*, **117,** 1779-1800.

Trapp, R. J., and M. L. Weisman, 2003: Low-level mesovortices within squall lines and bow echoes. Part II: Their genesis and implications. *Mon. Wea. Rev.*, **131,** 2804-2823.

Velden, C., and Coauthors, 2005: Recent innovations in deriving tropospheric winds from meteorological satellites. *Bull. Amer. Meteor. Soc.*, **86,** 205-223.

Wandishin, M. S., D. J. Stensrud, S. L. Mullen, and L. J. Wicker, 2010: On the predictability of mesoscale convective systems: Three-dimensional simulations. *Mon. Wea. Rev.*, **138,** 863-885.

--, --, --, and --, 2008: On the predictability of mesoscale convective systems: Two-dimensional simulations. *Wea. Forecasting*, **23,** 773-785.

Weisman, M. L., and Coauthors, 2015: The Mesoscale Predictability Experiment (MPEX). *Bull. Amer. Meteor. Soc.*, **96,** 2127-2149.

--, C. Evans, and L. F. Bosart, 2013: The 8 May 2009 superderecho: Analysis of a real-time explicit convective forecast. *Wea. Forecasting*, **28,** 863-892.

Wilson, J. W., and R. D. Roberts, 2006: Summary of convective storm initiation and evolution during IHOP: Observational and modeling perspective. *Mon. Wea. Rev.*, **134,** 23-47.

Xu, X., M. Xue, and Y. Wang, 2015a: The genesis of mesovortices within a real-data simulation of a bow echo system. *J. Atmos. Sci.*, **72,** 1963-1986.

--, --, and --, 2015b: Mesovortices within the 8 May 2009 bow echo over the central United States: Analyses of the characteristics and evolution based on Doppler radar observations and a high-resolution model simulation. *Mon. Wea. Rev.*, **143**, 2266-2290.

Zhang, C., Y. Wang, and K. Hamilton, 2011: Improved representation of boundary layer clouds over the southeast Pacific in ARW-WRF using a modified Tiedtke cumulus parameterization scheme. *Mon. Wea. Rev.*, **139,** 3489-3513.